Computational Investigation of a Boundary-Layer Ingesting Propulsion System for the Common Research Model

Brennan T. Blumenthal[1], Alaa Elmiligui[2], Karl A. Geiselhart[3], Richard L. Campbell[4]
NASA Langley Research Center, Hampton VA 23681

Mark D. Maughmer[5], Sven Schmitz[6]
Pennsylvania State University, University Park, PA 16802

The present paper examines potential propulsive and aerodynamic benefits of integrating a Boundary-Layer Ingestion (BLI) propulsion system into a typical commercial aircraft using the Common Research Model (CRM) geometry and the NASA Tetrahedral Unstructured Software System (TetrUSS). The Numerical Propulsion System Simulation (NPSS) environment is used to generate engine conditions for CFD analysis. Improvements to the BLI geometry are made using the Constrained Direct Iterative Surface Curvature (CDISC) design method. Previous studies have shown reductions of up to 25% in terms of propulsive power required for cruise for other axisymmetric geometries using the BLI concept. An analysis of engine power requirements, drag, and lift coefficients using the baseline and BLI geometries coupled with the NPSS model are shown. Potential benefits of the BLI system relating to cruise propulsive power are quantified using a power balance method, and a comparison to the baseline case is made. Iterations of the BLI geometric design are shown and any improvements between subsequent BLI designs presented. Simulations are conducted for a cruise flight condition of Mach 0.85 at an altitude of 38,500 feet and an angle of attack of 2° for all geometries. A comparison between available wind tunnel data, previous computational results, and the original CRM model is presented for model verification purposes along with full results for BLI power savings. Results indicate a 14.4% reduction in engine power requirements at cruise for the BLI configuration over the baseline geometry. Minor shaping of the aft portion of the fuselage using CDISC has been shown to increase the benefit from Boundary-Layer Ingestion further, resulting in a 15.6% reduction in power requirements for cruise as well as a drag reduction of eighteen counts over the baseline geometry.

Nomenclature

A_j	Jet exit area, ft^2	P_s	Shaft power, moving surfaces, lb_f/s
AR	Aspect Ratio	P_v	Volumetric Work, lb_f/s
C_D	Drag coefficient	p_{jet}	Static nozzle pressure
C_L	Lift coefficient	p_{0jet}	Total pressure of jet
C_m	Pitching moment coefficient	q_∞	Free-stream dynamic pressure, Pa
C_{Pk}	Net propulsor power coefficient	Re_c	Reynolds number based on mean aerodynamic chord
C_p	Pressure coefficient	S_{ref}	Geometry reference area, in^2
C_{ref}	Chord reference length	T	Thrust, lb_f
C_x	Net axial force coefficient	U	Potential energy, ft- lb_f
D	Drag force, lb_f	u	Flow velocity, ft/s
D_A	Drag due to airframe, lb_f	u_j	Flow velocity above free-stream, ft/s
F_x	Net streamwise axial force, lb_f	u_j'	Flow velocity above free-stream, BLI propulsor, ft/s
K	Kinetic energy, ft- lb_f	u_j''	Flow velocity at BLI propulsor exit
M	Mach number	u_w	Flow velocity of ingested wake, ft/s
$\dot{m}$	Mass flow rate, $slug/s$	u_∞	Free-stream velocity, ft/s
MP	Midplane	V	Velocity magnitude, ft/s
P	Power, lb_f/s	X_{ref}	Moment center in X-direction
P_k	Net mechanical power, propulsor faces, lb_f/s	Y_{ref}	Moment center in Y-direction

---

[1] Student Engineer, Configuration Aerodynamics Branch, Mail Stop 499, Member.
[2] Aerospace Engineer, Configuration Aerodynamics Branch, Mail Stop 499, Member.
[3] Aerospace Engineer, Aeronauticcs Systems Analysis Branch, Mail Stop 422, Associate Fellow.
[4] Aerospace Engineer, Configuration Aerodynamics Branch, Mail Stop 499, Member.
[5] Professor, Department of Aerospace Engineering, Associate Fellow
[6] Assistant Professor, Department of Aerospace Engineering, Senior Member

Z_{ref}	Moment center in Z-direction	ρ	Density, lb/ft^3	
α	Angle of attack, °	ϕ	Dissipation, $ft\text{-}lb_f$	
δ	Boundary-layer thickness, *inch*	Ω	Angular velocity, °/s	
η	Efficiency	$p_{0,\infty}$	Free-stream stagnation pressure, *psi*	
Λ	Taper ratio	p_0	Total pressure, *psi*	

Acronyms

BL	Boundary Layer	DPW	Drag Prediction Workshop
BLI	Boundary-Layer Ingestion	JAXA	Japan Aerospace Exploration Agency
BWB	Blended Wing Body	NPSS	Numerical Propulsion System Simulation
CAD	Computer Aided Design	DLR	German Aerospace Center
CDISC	Constrained Direct Iterative Surface Curvature	TetrUSS	Tetrahedral Unstructured Software System
CRM	Common Research Model	USM3D	Euler and Navier-Stokes flow solver
DLR	German Aerospace Center		

I. Introduction and Background

ONE of the goals of the NASA Subsonic Fixed Wing Project as part of the Fundamental Aeronautics program is to investigate technologies that may be able to improve flight performance for next-generation aircraft. Boundary-Layer Ingestion (BLI) is one such technology that has gained traction in recent years and is the focus of this paper. The concept of Boundary-Layer Ingestion has been around for several decades, with the first works published in the mid 1940s. In one of these early studies, Smith and Roberts[1] examined an aircraft that used suction slots located along the wing and fuselage to ingest the boundary layer in order to prevent or delay turbulent transition. In his study, Smith compared three engine configurations for the aircraft: a turbojet engine with boundary-layer suction, a turbojet, and a turboprop engine. Smith and Robert's tests showed that the engine, which included Boundary-Layer Ingestion, had a reduced fuel consumption of almost 33 percent as well as an increased C_L and L/D compared to the turbojet without Boundary-Layer Ingestion for the same aircraft.

In the 1980s, Goldschmied[2] designed a small integrated, self-propelled wind-tunnel model using a concept referred to as the Goldschmied propulsor. This propulsor included a slot around the aft portion of the fuselage to allow for Boundary-Layer Ingestion. Wind-tunnel testing was conducted with this model, both in an unpowered and in a boundary-layer ingesting configuration. Using the data collected from the wind tunnel, Goldschmied was able to show that ingesting the boundary-layer allowed for a propulsion power reduction of 50 percent over the unpowered configuration; however, recently an attempt to recreate these wind tunnel test results for propulsion power reduction at the California Polytechnic State University wind tunnel using a Goldschmied propulsor proved unsuccessful[3].

In the 1970s, Douglas[4] conducted a study of aircraft with and without Boundary-Layer Ingestion. Although Douglas made some assumptions about the compressibility of the flow, inlet losses and the conditions at which it entered the engine, he was able to show that the Boundary-Layer Ingestion resulted in a reduction of the kinetic energy of the wake and the jet, resulting in a propulsive efficiency improvement of 16 percent over the non-ingesting aircraft.

More recent studies have combined Boundary-Layer Ingestion technology with blended wing body (BWB) geometry configurations in order to reduce specific fuel consumption for the aircraft[5-7]. These studies all show a reduction in the mechanical power required by the propulsor as compared to a typical podded nacelle configuration.

A recent experimental investigation conducted by Drela into the merits of Boundary-Layer Ingestion using an electric ducted fan propulsor mounted behind an NACA 0040 body of revolution showed a power savings benefit of 25 percent over the baseline, non boundary-layer ingesting case[8].

There have also been several studies focused on assessing and reducing flow distortions at the fan inlet face, which could affect engine efficiency and therefore overall performance of a boundary-layer ingesting system[6,9,10]. However, this study will focus on quantifying the aerodynamic benefit of BLI for the Common Research Model (CRM) geometry rather than BLI effects on engine performance.

The main objective of this paper is to computationally verify if there is any benefit in terms of reduced propulsive power requirements and drag reduction to be gained from implementing BLI on a conventional commercial aircraft geometry, as well as to quantify and make a 1st round attempt to improve on any such benefit. The principle success criteria for this work is to determine whether such a system might yield a net aerodynamic or propulsive benefit and whether this topic warrants additional study.

II. Boundary-Layer Ingestion Theory (Quasi One-Dimensional)

The main principle of this BLI concept for the purposes of this study is to reduce the overall propulsive power required by the aircraft by integrating an additional propulsor in the aft section of the fuselage, where the lower velocity boundary layer can be ingested by the engine intake.

The BLI concept is derived from the more general concept of wake ingestion, which has been in use in marine propulsion for a number of years[11]. By re-energizing the wake produced by the airframe through the use of Boundary-Layer Ingestion, overall energy waste can be decreased, thus allowing the aircraft to move through the air with less propulsive power than would be required with current podded nacelle configurations. The potential benefit of BLI can be understood by considering three configurations (as shown in Fig. 1): a typical, underwing podded nacelle geometry with no Boundary-Layer Ingestion (Baseline Configuration - top); a configuration with only a BLI propulsor (Ideal BLI Configuration – middle); and a more realistic configuration with both underwing and BLI propulsors (Actual BLI Configuration - bottom).
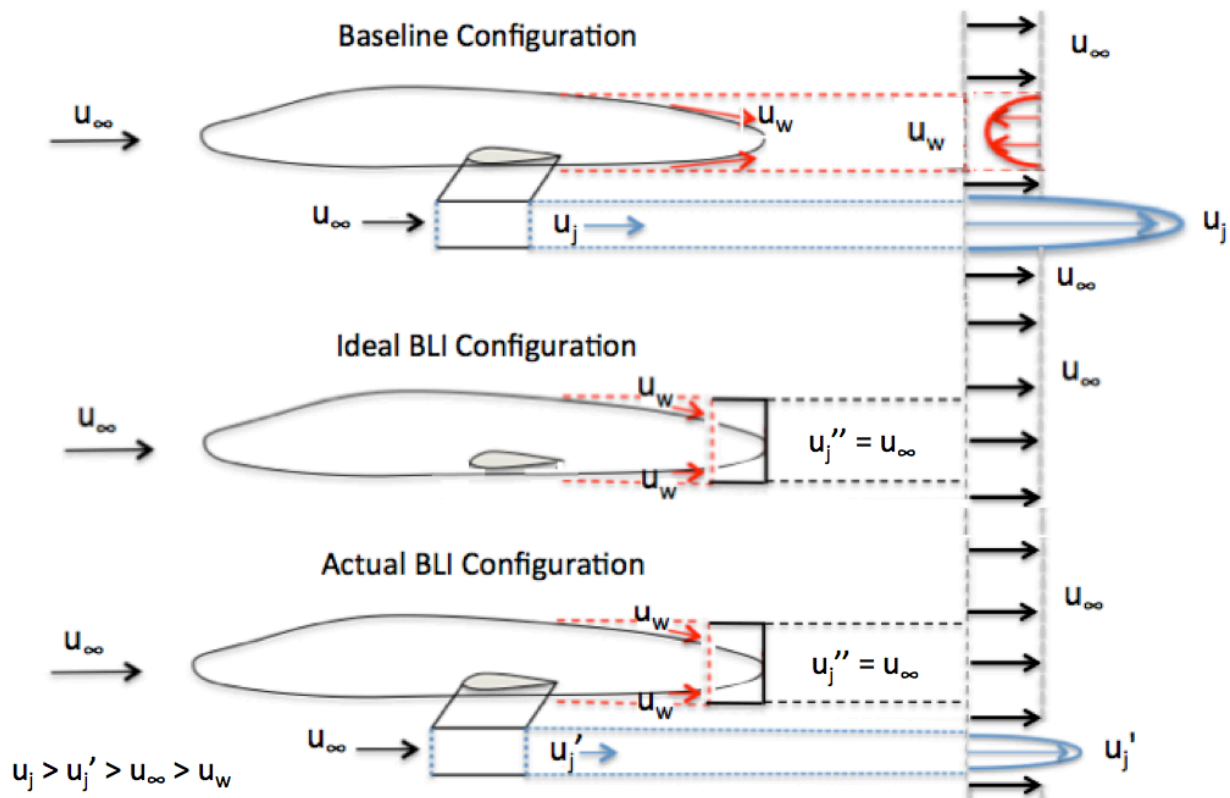

Figure 1: Conceptual benefit of BLI – baseline geometry versus idealized and actual BLI geometries.

Derivation of non-BLI Power Requirements

In the Ideal BLI Configuration, it is assumed that one hundred percent of the wake is ingested by the propulsor and that the wake is perfectly filled. However, as it would likely not be possible, nor beneficial to ingest one hundred percent of the developing boundary layer/wake, the actual BLI configuration would require supplemental propulsion from an underwing nacelle, as shown in the Actual BLI Configuration. In addition, there would likely be a variety of safety issues that would arise from a configuration with just a single BLI propulsor. Although the focus of this work is on an 'Actual' BLI configuration with both BLI and underwing propulsors, for simplicity, the following derivation will compare the Baseline Configuration (top) to an Ideal BLI Configuration (middle). The drag from the wing was ignored in all cases, as the focus of this work is fuselage boundary layer ingestion.

For the typical podded nacelle geometry, the airflow enters the engine at free-stream velocity, u_∞. The engine then accelerates the flow to a velocity u_j, which is higher than free-stream velocity in order to balance out the momentum deficit created by the airframe drag. For the BLI geometry, instead of ingesting the free-stream flow, the

engine ingests the slower moving boundary-layer flow, u_w, and accelerates the flow up to free-stream velocity, u_∞. The potential benefit of a BLI system is derived from the difference in required energy input between BLI and non-BLI geometries by the aircraft engines to achieve the same net axial force.[12,13] This benefit can be assessed starting with the general thrust equation

$$Thrust, \ T = (\dot{m} * u)_j - (\dot{m} * u)_\infty + (p_j - p_\infty) * A_j \tag{1}$$

where p_j and p_∞ are defined as the exit and free-stream pressures, respectively. A_j is defined as the jet exit area and u_j and u_∞ are the jet exit velocity and free-stream velocity, respectively. For a gas turbine engine, the nozzle of the turbine is usually designed in such a way as to make the exit pressure equal to free-stream pressure. In this case, the pressure-area term of the general thrust equation will equal zero and can be dropped. The thrust equation can then be written as

$$T = (\dot{m} * u)_j - (\dot{m} * u)_\infty \tag{2}$$

To simplify the derivation, the added fuel used for combustion and the bleed air will be neglected. Thus, the exit mass flow rate will be assumed to be equal to the free-stream mass flow rate. From this, Eq. (2) can be rewritten as

$$T = \dot{m} * (u_j - u_\infty) \tag{3}$$

For cruise conditions, this total net axial force (thrust) is equal to the overall drag force of the aircraft, D_A. In addition, u_w is defined as the velocity of the ingested wake.

$$T = \dot{m} * (u_j - u_\infty) = \dot{m} * (u_\infty - u_w) = D_A \tag{4}$$

Next, the total energy added to the system, $E_{mechanical}$ is defined as the sum of potential energy, U, and kinetic energy, K.

$$E_{mechanical} = U + K \tag{5}$$

Since there is no change in potential energy of the system, the total mechanical energy added to the system is equal to the kinetic energy, K, added to the system by the engine, which can then be written as

$$E_{mechanical} = K = \frac{1}{2} * m * u^2 \tag{6}$$

The total change in kinetic energy for the non-BLI case can then be written as the difference between the free-stream velocity, u_∞, and the jet engine exit velocity, u_j.

$$E_{Mechanical,added} = \frac{1}{2} * m * u_j^2 - \frac{1}{2} * m * u_\infty^2 = \frac{1}{2} * m * (u_j^2 - u_\infty^2) \tag{7}$$

The rate at which this mechanical energy is added to the flow (Power), P, can then be obtained by substituting in the mass flow rate, $\dot{m}$.

$$P_{added,non-BLI} = \frac{1}{2} * \dot{m} * (u_j^2 - u_\infty^2) \tag{8}$$

Equation (8) can be rewritten as

$$P_{added,non-BLI} = \frac{1}{2} * \dot{m} * (u_j - u_\infty) * (u_j + u_\infty) \tag{9}$$

Substituting Eq. (3) in above, the rate at which mechanical energy is added to the non-BLI system can be written as

$$P_{added,non-BLI} = \frac{T}{2} * (u_j + u_\infty) \tag{10}$$

The (useful) power required for flight is defined as

$$P_{required} = D_A * u_\infty \tag{11}$$

and substituting in Eq. (4) for D_A,

$$P_{required} = \dot{m} * (u_j - u_\infty) * u_\infty \tag{12}$$

Derivation of BLI Power Requirements
For the BLI concept, the assumption that 100% of the boundary layer is ingested by the engine and accelerated back up to free-stream velocity was made. In addition, an assumption that the non-BLI and BLI cases will have

equivalent mass flow rates was made. This assumption will be discussed in further detail in subsequent sections. Starting with Equation (1) but substituting in for the BLI case (middle sketch in Fig. 1) gives

$$Thrust, T = \dot{m} * \left(u_j^{''} - u_\infty\right) = \dot{m} * (u_\infty - u_w) = D_A \tag{13}$$

Where $u_j^{''}$ is the jet exhaust velocity from the BLI engine, which is assumed to be equal to freestream velocity, u_∞.

The rate at which energy is added to the flow by the BLI engine is

$$P_{added,\ BLI} = \frac{\dot{m}}{2} * (u_\infty^2 - u_w^2) = \frac{T}{2} * (u_w + u_\infty) \tag{14}$$

The required power for flight for the BLI geometry is the same as for the podded nacelle

$$P_{required} = D_A * u_\infty = \dot{m} * (u_\infty - u_w) * u_\infty \tag{15}$$

A comparison of Eqs. (14) and (10) show that

$$\frac{T}{2} * (u_w + u_\infty) < \frac{T}{2} * (u_j + u_\infty) \tag{16}$$

since $u_w \leq u_j$, then

$$P_{required,BLI} < P_{required,non-BLI}$$

From this, it is evident that less propulsive power is required by the Boundary-Layer Ingestion configuration than the conventional underwing configuration to maintain the same axial force and assuming the same mass-flow rate.

The difference in energy input between the BLI and non-BLI scenario arises due to the fact that for a specific required force, less power needs to be added to a flow that enters the engine at a lower velocity.

The assumption of equal mass-flow rates for the BLI and non-BLI cases will not hold when trying to directly compare a BLI propulsor to a propulsor in free-stream. The boundary-layer flow will have a lower mass-flow rate by virtue of its velocity being lower than that of the free-stream flow. The assumption of equal mass-flow rates is instead based on the notion that the BLI propulsor will only be able to ingest a certain percentage of mass flow that the free-stream propulsor can. This percentage of the free-stream mass-flow rate is assumed to be the point of comparison for the equal mass-flow rate assumption in the equations above. For example, assume that a free-stream propulsor has a mass flow rate of 20 kg/s but a BLI propulsor can ingest only 5 kg/s. The 5 kg/s is assumed to be the point of comparison for equal mass-flow rates, $\dot{m}$, in the equations above. This means that although the BLI propulsor can ingest only a portion of the mass-flow that the free-stream propulsor can, this smaller portion is used more efficiently in the BLI case compared to the non-BLI case and results in a lower energy input for the BLI system to produce the same amount of thrust as the non-BLI system. This will be discussed in further detail in subsequent sections.

Consider an engine where the flow enters at a velocity u_∞ and exits at a velocity u_j. As shown in Eq. (3), the thrust created by the engine is

$$T = \dot{m}\Delta u = \dot{m} * (u_j - u_\infty) \tag{17}$$

As in Eq. (8), the power added to the flow by the engine is

$$P_{added} = \frac{\dot{m}}{2}\left(u_j^2 - u_\infty^2\right) \tag{18}$$

Substituting Eq. (17) in above yields

$$P_{added} = T * \frac{u_\infty + u_j}{2} = T * \left(u_\infty + \frac{\Delta u}{2}\right) \tag{19}$$

From Eqs. (17) and (19), it can be seen that for a constant mass-flow rate and desired propulsive force, Δu is constant. A decrease in the intake velocity, u_∞, which would be achieved by ingesting the boundary-layer flow that is moving slower than the free-stream flow than an underwing engine would see, results in a decrease in the amount of power that needs to be added to the flow by the propulsion system in order to achieve that same desired propulsive force. It is important to note, however, that this analysis does not take into account various losses that would be expected due to the non-uniform velocity distribution of the boundary layer, various engine efficiencies (fan, compressors, etc.) and increases in wetted area due to implementation of a BLI system[14]. A more robust, two-dimensional derivation of BLI power requirements can be found in the first author's thesis[15].

III. Baseline Geometry and Engine Model Generation − Underwing

The baseline geometry used for the purposes of this study is the Common Research Model (CRM)[16]. The Common Research Model was developed by a consortium of both public and private sector groups including, but not limited to, Boeing, Cessna, JAXA (Japan Aerospace Exploration Agency) and DLR (German Aerospace Center), in conjunction with NASA in order to help develop computational fluid dynamic (CFD) applications and validate their results.

The Common Research Model geometry itself is representative of a typical transonic transportation aircraft designed for a Mach number of M=0.85 with a nominal lift coefficient of C_L=0.50, a Reynolds number of Re_c=40 million per reference chord, and an aspect-ratio of AR=9.0. The geometry and data, including all wind-tunnel tests and CFD results associated with the Common Research Model, are all open-source and available to the public[16].

Table 1: Reference quantities for CRM geometry.

S_{ref}	594,720.0 in^2
Trap-Wing Area	576,000.0 in^2
C_{ref}	275.80 in
Span	2313.50 in
X_{ref}	1325.90 in
Y_{ref}	468.75 in
Z_{ref}	177.95 in
Λ	0.275
AR	9

The most recent baseline CRM geometry consists of a tube-like body, wing, nacelle, pylon, and horizontal tail. However, there are various configurations of the CRM geometry available, which do not include some of these features[17].
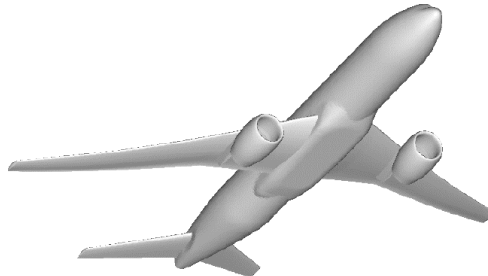
Figure 4: Full Common Research Model geometry.

For the purposes of this study, a semispan geometry consisting of the aircraft fuselage, wing, underwing nacelle, and horizontal tail are used. A semispan model is used in order to save computational resources. The boundary-layer ingesting system will be placed downstream of the horizontal tail. At this time, the underwing nacelle on the CRM is flow-through only and does not have any internal engine geometry.

In order to determine the existence of and quantify any potential benefit that might arise through the use of BLI, it is necessary to develop a working engine model for the underwing engine. The USM3D flow solver, which will be discussed in subsequent sections, allows for the modeling of jet engines through the use of inflow, core outflow, and fan bypass outflow boundary conditions defined on the solid model geometry prior to grid generation. As the CRM model currently uses flow-through nacelles and does not have any engine geometry, a model based on publically available engine geometry for the GE90-115B, the PAX300, will be added to the CRM underwing nacelle[18].

The internal engine geometry will consist of an inlet hub, inflow plane (green), core exit (red), bypass fan exit (yellow) and plug sections as shown in Fig. 5 below.

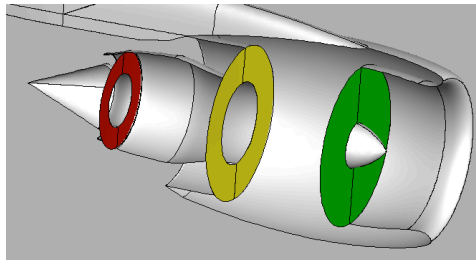American Institute of Aeronautics and Astronautics

Figure 5: Internal view of underwing nacelle geometry and boundary condition planes.

It is not necessary or practical to model the various compressors, ducts, and other components of the engine in USM3D, as this is done in the Numerical Propulsion System Simulation (NPSS). Engine conditions are specified by the user and applied to the core exit and bypass fan exit faces of the engine[19].

The inflow engine parameters are determined automatically within USM3D through a mass-flux balance method, with the fan and jet flows determined by adjusting the average back pressure across the inlet face. Using an averaged back pressure, the mass flux is balanced, and distortion on the plane is maintained. The outflow conditions for the engine are determined through nondimensional user-prescribed inputs for the static nozzle pressure. These six variables, three for each exit section, are calculated using the NPSS model and input into USM3D.

The PAX300 NPSS engine model, developed at NASA Glenn and used previously to model a GE90-115B similar engine[20] is used to generate the above USM3D inputs. The amount of thrust that the engine model produces is throttled in order to attain cruise conditions and provide a point of comparison between the BLI and non-BLI systems. Fig. 6 shows a schematic of the engine geometry.
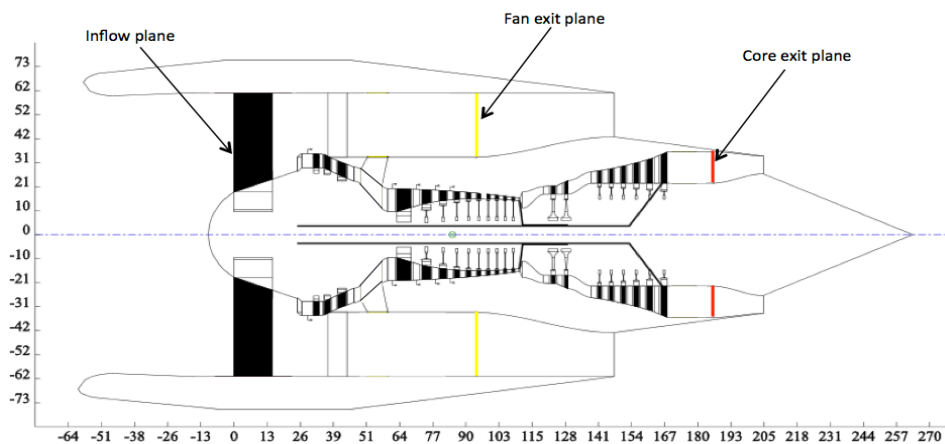
Figure 6: Geometry of NPSS model (inches).

Fig. 7 below shows the semispan CRM with added internal engine geometry, which serves as the baseline geometry for this study. An open actuator disc, which will be discussed further in the following sections, is used to model the BLI system.
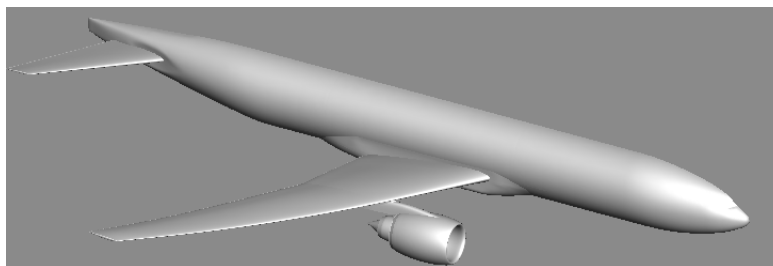
Figure 7: Baseline geometry – the Common Research Model with internal engine geometry.

American Institute of Aeronautics and Astronautics

IV. Assessing the BLI Benefit

To assess the potential benefit of BLI, the baseline geometry with underwing engines, shown in Fig. 7 is compared to the integrated BLI geometry, shown in Fig. 25. Computations are performed for both the baseline and BLI geometries and compared to determine the potential BLI benefit. This potential benefit will be assessed via a power balance method outlined by Drela[21].

For this method, the benefit of BLI will be derived from reducing the power dissipation in the overall flow field by reducing streamwise velocities and wasted kinetic energy by the aircraft. This is accomplished by filling in the wake generated by the airframe with the BLI propulsor, as shown in Fig. 1. This power balance method allows for the unification of boundary-layer losses and propulsor losses of the aircraft, rather than attempting to tediously separate out the thrust and drag forces on the aircraft. The potential benefit of a BLI system is likely to be affected by the fan performance of the engine due to distorted flow at the inlet of the propulsor. Drela's power balance method allows for the separation of the fan efficiency from the propulsive efficiency of the aircraft, thus allowing for an easier assessment of potential benefit.

There are three sources of mechanical power within a flow field as outlined by Drela: P_k, which is the net mechanical power across the propulsor inflow and outflow faces, P_s, which is shaft power from moving surfaces, and P_v, which is the power due to the volumetric work within a flow field. For a control volume encompassing the propulsor and in the low-speed case, the only flow field power source left is P_k, which can be defined as the volume flux of total pressure across the inflow and outflow faces of the engine

$$P_k = \oiint \left(p_{0_\infty} - p_0\right) V \cdot \hat{n} \, dS \tag{20}$$

where p_0 is the total pressure at the engine face, p_{0_∞} is the free-stream total pressure, V is the inlet velocity at the propulsor face, and $\hat{n}$ is the vector normal to the fan face. The area integral is taken over both inflow and outflow propulsor planes, so P_k is a measure of net engine flow power while internal propulsor losses are irrelevant, allowing the engine fan efficiency to be separated from the aerodynamics of the BLI geometry[21].

Since thrust and drag forces are difficult to separate out for a BLI system, the net streamwise force, F_x, is used to aid in the analysis. A nondimensional net streamwise force coefficient, C_x, will also be defined as follows.

$$C_x = \frac{F_x}{q_\infty S_{ref}} \tag{21}$$

where q_∞ is the free-stream dynamic pressure and S_{ref} is the reference area of the geometry.

$$C_{P_k} = \frac{P_K}{q_\infty V_\infty S_{ref}} \tag{22}$$

As S_{ref} may change between geometry iterations, a dimensionless net propulsor power coefficient, C_{p_k}, is defined to allow for effective comparison between non-BLI and BLI geometries using the net mechanical power, P_k defined previously in Eq. (20).

The aerodynamic benefit of the BLI system can be expressed as follows

$$BLI\ benefit = \frac{(C_{p_k})_{non-BLI} - (C_{p_k})_{BLI}}{(C_{p_k})_{non-BLI}} \tag{23}$$

V. Computational Tools

Several different computational tools, outlined below, were used for this study.

Grid Generation

The surface triangulations along with the field tetrahedral volume grids were generated using the GridTool and VGRID software developed at LaRC[22]. GridTool serves as a connection between Computer Aided Design (CAD) software and grid generation software such as VGRID. In GridTool, surface patches are defined along the configuration by the user, source terms are places throughout the domain for grid generation, and domain boundaries for the model are defined. A rectangular box that encompasses the geometry is used to define the computational domain and far-field boundaries. Each face of this rectangular box is located ten body lengths away from the configuration in the upstream, radial, and downstream directions. The output from GridTool is used to automatically generate the computational domain using VGRID. VGRID uses an advancing front method for generating Euler tetrahedral grids and an advancing layers method for thin-layer viscous grid generation for Navier-Stokes analysis.

As a general practice, each final converged solution is analyzed to ensure that the viscous sublayer, has been grid resolved and that the average y^+ is less than 1.

Numerical Propulsion System Simulation

NPSS is a component-based, object-oriented, engine cycle simulator capable of simulating the aerothermodynamic cycle for gas turbine engines and other complex systems. The system uses a linked building block approach to define system configuration that allows for single and multi-point design as well as steady-state and transient analyses. NPSS focuses on the integration of aerodynamics, structures, and heat transfer along with the concept of numerical zooming between zero-dimensional, one, two, and three-dimensional engine codes[23,24]. An engine model similar to the GE90-115B, the PAX300[25], will be used in this work to generate engine conditions for the underwing engine for use in CFD analysis.

USM3D Flow Solver

USM3D is a tetrahedral cell-centered, finite-volume, Euler and Navier-Stokes flow solver. Time integration follows the implicit point Gauss-Seidel algorithm, explicit Runge-Kutta approach, and local time stepping for convergence acceleration[19]. For this study, Roe's flux-difference splitting (FDS) method along with the Spalart-Allmaras turbulence model with no flux limiter is used. Separate core, bypass and inflow boundary conditions are used to model the underwing engine. Inflow engine parameters are determined automatically within USM3D through a mass-flux balance method with the fan and jet flows by adjusting the average back pressure across the inlet face. Using an averaged back pressure, the mass flux is balanced, and distortion on the plane is maintained. The outflow conditions for the engine are determined through nondimensional user-prescribed inputs for static nozzle pressure, p_{jet}, stagnation pressure of the jet, p_{0jet}, and stagnation temperature of the jet, T_{0jet}, for both the core and bypass fan flows. These user-prescribed inputs will be calculated from NPSS model output.

Constrained Direct Iterative Surface Curvature

CDISC is a knowledge-based inverse design approach. Geometry and flow information from a preliminary analysis is passed from the flow solver to the CDISC module. Surface coordinates and pressure coefficients are extracted from the analysis, and an initial set of target pressures are generated using the current analysis pressures. These target pressures are automatically adjusted to meet the input flow constraints, and a new surface geometry is obtained. The volume grid is then modified based on surface geometry changes and input back into the flow solver for further analysis. This iterative process repeats until the extracted surface pressures match input target pressures[26].
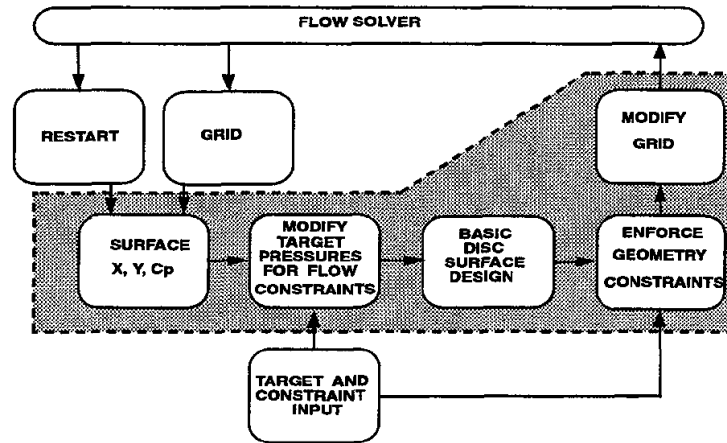

Figure 8: CDISC system flow chart[26].

VI.   Methodology Overview

In order to determine the aerodynamic effects and potential benefits of a Boundary-Layer Ingestion system on the Common Research Model (CRM), several different iterations of the CRM geometry were used. The baseline geometry consists of an unaltered semispan CRM geometry incorporating an underwing nacelle with added internal engine geometry, as shown in Fig. 7. Unstructured viscous grids were generated using NASA Langley's GridTool and VGRID grid generation packages. The Numerical Propulsion System Simulation (NPSS) software was used to

simulate an engine cycle similar to that of the GE90-115B gas turbine engine at cruise conditions using publicly available data. This engine simulation was used to determine the engine inlet and exit boundary conditions for the underwing nacelle. USM3D was used as the flow solver. Each geometry was run for a total of 25,000 iterations on the NASA Pleiades supercomputer in order to ensure solution convergence. The model was run at cruise conditions of Mach 0.85 and an altitude of 38500 feet with 2° angle of attack and no sideslip condition. As outlined previously, net propulsor power and net horizontal force coefficients were calculated.

After the baseline run calculations were completed, the CRM geometry was altered to incorporate the BLI system. For this, an actuator disc was placed at the approximate fan location slightly downstream of the empennage of the fuselage to represent the BLI system. The rest of the geometry, including underwing nacelle, remained unchanged. The same cruise conditions outlined above were used and once again, the net propulsor power, net horizontal force, and drag coefficients were calculated.

Once the first BLI run was completed, the BLI-integrated geometry was modified in an attempt to optimize the flow? and potential benefits of the system. The exact changes to the geometry are discussed in detail in later sections. These changes to the BLI geometric design were made using CDISC.

Once all of the simulations were completed, any aerodynamic or propulsive power savings benefit from the BLI system as compared to the non-BLI configuration were determined. An assessment of the BLI concept for this application was made and future work recommended.

VII.   Methodology for Comparison of Baseline (Non-BLI) and BLI Geometries

For an equivalent mass-flow rate, it has been shown in Section II that a BLI system requires less propulsive power than a conventional non-BLI system to achieve the same desired axial force. However, since the BLI system by definition ingests the slower-moving boundary-layer air, it is difficult and impractical to actually design the BLI system in such a way as to have the same mass-flow rate as that of an underwing engine. Instead, the BLI system is constrained so as to ingest only the mass flow present in the developing boundary layer and accelerate it up to free-stream velocity as a way to supplement thrust generated by the underwing engines instead of attempting to replace them. This has several implications: 1) a portion of the overall required thrust for cruise will now be produced more efficiently by the BLI system compared to the underwing engine, 2) the underwing engine now needs to produce less thrust overall since the BLI system is contributing a portion of the total thrust required, which should reduce the amount of propulsive power required by the underwing engine, and 3) since the BLI system is ingesting and accelerating the boundary-layer air, there should be some benefit in terms of reduced drag on the fuselage that would not be present in a conventional propulsive system, although this will likely be dependent on the actual geometry alterations made to incorporate the BLI system. At that point, the underwing engine could possible be made smaller, thus further reducing aircraft drag and increasing the overall benefit of the BLI system.

In order to fairly compare the required propulsive power for the BLI and non-BLI systems at cruise, the net axial force coefficient, C_X, is constrained to be zero for all configurations. C_X is computed by summing the axial component of the integrated pressure and viscous forces on all airframe surfaces. The BLI engine is modeled to ingest the developing boundary layer and accelerate it up to free-stream velocity, while the underwing engine will be modeled using the parameters derived from the NPSS model and adjusted accordingly, in order to achieve a zero net axial force for the aircraft.

VIII.   USM3D Code Validation Study

In order to determine the validity of the computational results pertaining to potential benefits of BLI using the CRM with added internal engine geometry obtained in this study, it is first necessary to compare computational results for an unaltered CRM geometry to previous computational results and available wind-tunnel test data. Previous experimental investigations using a variant of the CRM geometry with no underwing nacelle have been completed at the NASA Langley Research Center National Transonic Facility (NTF) as part of the Drag Prediction Workshop (DPW) series. The data obtained through these experimental investigations are available online as part of the Common Research Model project and will be used for CFD verification[15-17].
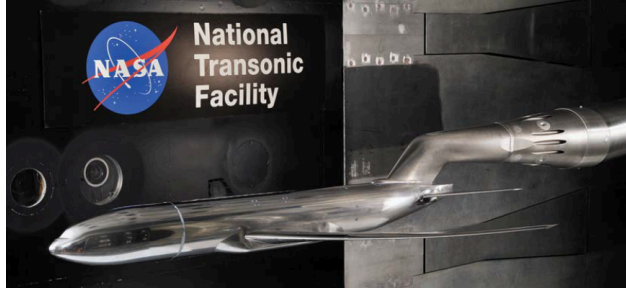
Figure 9: Photo of the Common Research Model in the National Transonic Facility.

Testing was conducted at Reynolds numbers of 5, 19.8, and 30 million based on mean aerodynamic chord with temperatures ranging from -250°F to 120°F and free-stream Mach numbers ranging from 0.7 to 0.87. Data were collected over an angle-of-attack range of -3° to 12° for Reynolds number of 5 million based on mean aerodynamic chord. For the purposes of this study, NTF data obtained at a Reynolds number of 5 million based on mean aerodynamic chord and a Mach number of 0.85 were used.

For the computational model, the GridTool and VGRID software packages were used to generate an unstructured tetrahedral grid for the wing/body/tail CRM geometry. The surface mesh for the baseline geometry consisted of a total of 65 surface patches with a volume grid size of approximately 26.2 million unstructured tetrahedral cells with a y+ value < 1. The computational domain extended roughly 10 body lengths from the airframe in all directions. A total of twenty-five thousand iterations were run for each angle-of-attack case. The computational model used first-order spatial accuracy for the first five thousand iterations in order to overcome any initial transients in the model and second-order accuracy for the final twenty thousand iterations. Simulations were run over a range of angles of attack from 0° to 5° at a Reynolds number of 5 million based on mean aerodynamic chord (7.45 inches). A symmetry plane was used over the semispan of the geometry in order to reduce computational time. All models were run on the NASA Ames Pleiades supercomputer using 136 processors. Solutions typically required about 17 hours of wall-clock time. Solution convergence was assessed by tracking the convergence parameter using the L2-norm solution residual of all flow variables, $\log(r/r_0)$, versus iteration. Fig. 10 shows the solution convergence for one of the cases. As the solution seems to be fully converged after fifteen thousand iterations, it is likely possible to reduce the total number of solution iterations and wall clock time, thus saving on computational resources. The simulation starts with first-order and switches to second-order order after five thousand iterations. The residual spikes at this point but quickly drops several orders of magnitude and converges asymptotically after an additional ten thousand iterations. Forces and moments were computed by the USM3D flow solver by computing skin friction and pressure on each of the user-defined patches and summing over the entire geometry.
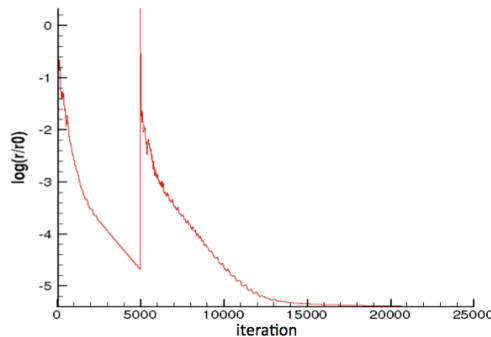

Figure 10: L2-norm solution convergence for computational model.

IX. USM3D Code Validation – Results and Discussion

This study consisted of comparing computational cases run at a Mach number of 0.85 and Reynolds number of 5 million, based on mean aerodynamic chord, and wind tunnel data from the NASA Langley National Transonic Facility taken at the same conditions, along with previous computational results obtained from the fourth and fifth AIAA Drag Prediction Workshop[28,29]. A summary of computational results obtained from this study for drag, lift,

and pitching moment coefficients, respectively, are shown below. All associated wind-tunnel data and previous computational results can be found online as part of the Drag Prediction Workshop series[28,29].

Table 2: Summary of USM3D computational results – verification study.

Mach	α	C_L	C_D	C_m
0.85	0.0	0.17492	0.01849	0.05002
0.85	1.0	0.31589	0.02099	-0.00042
0.85	1.5	0.38716	0.02293	-0.02281
0.85	2.0	0.46206	0.02552	-0.04416
0.85	2.5	0.53781	0.02954	-0.06608
0.85	3.0	0.60133	0.03548	-0.07838
0.85	3.5	0.64361	0.04282	-0.07220
0.85	4.0	0.67862	0.05122	-0.06109
0.85	4.5	0.70213	0.05912	-0.06602
0.85	5.0	0.72612	0.06805	-0.06327

Figures 11, 12, and 13, show a comparison of the computational results for the baseline geometry (shown as Current USM3D) and previously obtained computational results (shown as Previous USM3D – Original) plotted against the NTF data (T197R74, T197R79, and T197R81) to verify the accuracy of the baseline CFD model for this study.
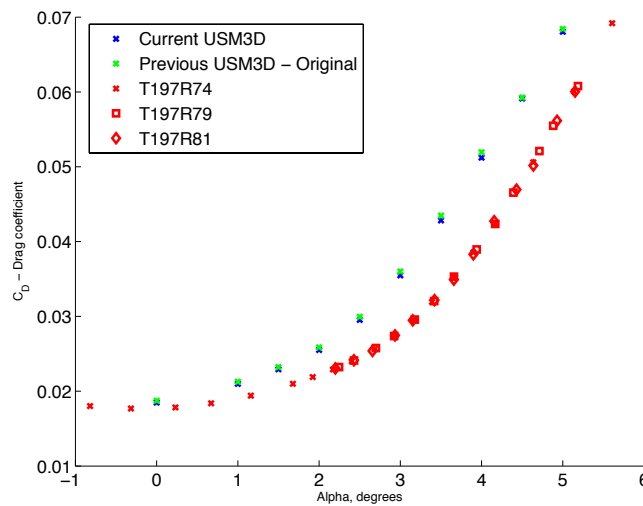
Figure 11: Comparison of USM3D results and NTF data for C_D, (Re_c=5 million, M=0.85).
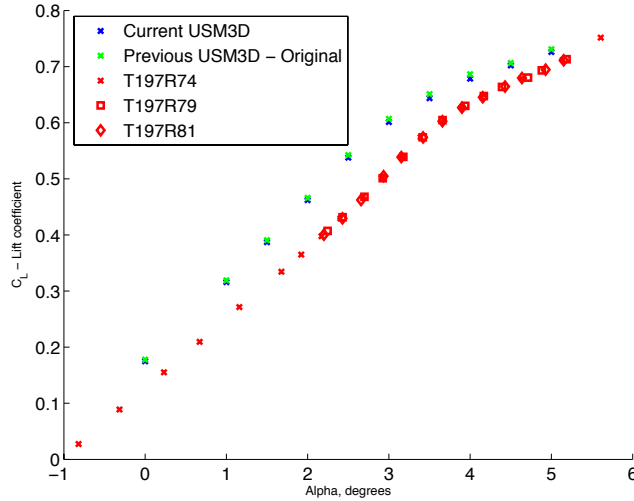
Figure 12: Comparison of USM3D results and NTF data for C_L, (Re_c=5 million, M=0.85).
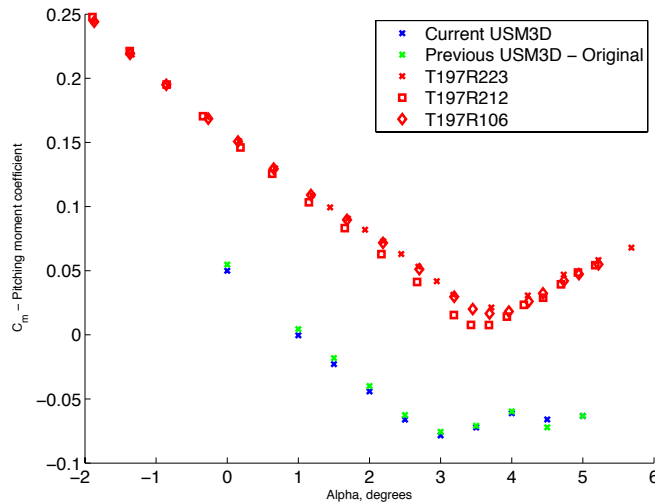
Figure 13: Comparison of USM3D results and NTF data for C_m, (Re_c=5 million, M=0.85).

A comparison of computational results obtained for verification purposes (blue) for the drag coefficient, (Fig. 11) lift coefficient, (Fig. 12) and pitching moment coefficient (Fig. 13) show a very good agreement with previous computational results (green) for all angles of attack. Both sets of computational results predict up to approximately 0.01 higher drag coefficient, C_D, for all angles attack compared to available NTF data (red) as well as up to approximately 0.08 higher lift coefficient, C_L. Although the computational models predict similar values for the pitching moment coefficient, C_m, there is a large discrepancy compared to the wind tunnel data, with poor agreement for all angles of attack shown. The original wind tunnel testing was conducted as part of the fourth AIAA Drag Prediction Workshop[28]. After the wind-tunnel testing was completed, a large discrepancy between wind-tunnel data and computational models was observed[29], similar to the above results. These results were first attributed to aeroelastic wing bending of the tunnel model that was not modeled in the computational cases. Further investigation into the wind-tunnel test data revealed interference effects from the wind tunnel support system as at least part of the reason for the discrepancy, especially in the pitching moment coefficient[28,29].

Overall, apart from the pitching moment coefficient results, there is a reasonable agreement between the computational results and available wind tunnel data. As such, the computational results obtained in this study are considered to be validated against CFD results obtained during the Drag Prediction Workshop.

X. Underwing Engine Model CFD Results

The semispan CRM geometry with underwing nacelle and internal engine geometry, discussed previously in Section III, was used as the baseline geometry for this study. Cruise conditions as outlined in Section VI were used for the simulation. All simulations were conducted at a Reynolds number of 5 million based on mean aerodynamic chord.

While the main focus of this work is not to redesign or optimize the underwing engine, the ability to couple the NPSS raw output with the USM3D flow solver to produce a realistic representation of a high bypass turbofan engine is a key part of determining proof-of-concept for BLI in this application.

Figs. 14 and 15 show a two-dimensional, centerline cut through the underwing engine. From this, it can be seen that the flow-through engine inlet is subsonic with no shocks apparent. Fig. 16 shows a Mach contour at the engine inlet face with a maximum Mach number of less than 0.6, indicating a good inlet design. The exit flow is close to Mach 1, which is desirable for high bypass turbofan engines. In addition, there does appear to be a small low-speed zone near the engine plug, which could be reduced by making the plug larger. However, as this zone is relatively small and the intent is to investigate BLI and not optimize the underwing engine, the plug dimensions will remain unchanged. Overall, the NPSS model yielded good results and allows for a reasonable assessment of BLI in this application.
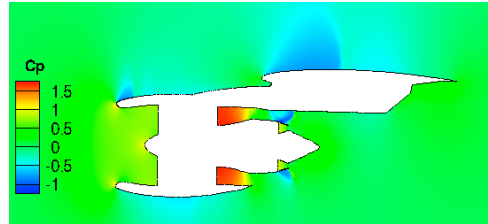
Figure 14: Underwing engine, C_p contour plot, (Re$_c$=5 million, M=0.85, α = 2°).
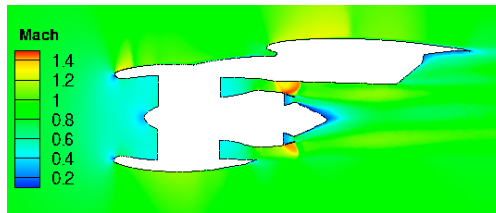
Figure 15: Underwing engine, Mach number contour plot, (Re$_c$=5 million, M=0.85, α = 2°).
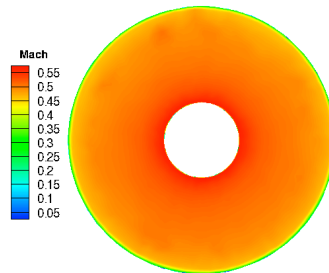
Figure 16: Underwing engine, Mach number contour plot – inlet face, (Re$_c$=5 million, M=0.85, α = 2°).

XI. Baseline Geometry CRM and Underwing Engine Model CFD Results – Power, Drag and Thrust

As defined in Section IV, axial force, drag, and net propulsor power coefficients were calculated for the baseline geometry and are presented below. The axial force coefficient, C_x, was computed over all surfaces. The drag coefficient, C_D, was computed over only the solid surfaces, and the engine power coefficient, C_{P_K}, was computed over the engine inlet, bypass exit, and core exit faces. The amount of thrust that the engine model produces was throttled in order to gather the necessary data.

Table 3: Computed axial force, drag and engine power coefficients for baseline (Re$_c$=5 million, M=0.85, α = 2°).

Thrust (lbf)	C$_x$	C$_D$	C_{P_k}
9076.9	-0.00145	0.0404	1.785
8509.5	-0.00041	0.0393	1.656
7942.5	0.00055	0.0383	1.463

From Table 3, it can be seen that C_x transitions from a negative to a positive value. This sign change denotes a change from a net acceleration to net deceleration based on the coordinate system used. Due to the fidelity of the engine model, it is not possible to refine the engine conditions any further between these two points, so an estimate of C_{P_k}, C_D, and the thrust at the exact cruise point of $C_x = 0$, must be interpolated from available data.
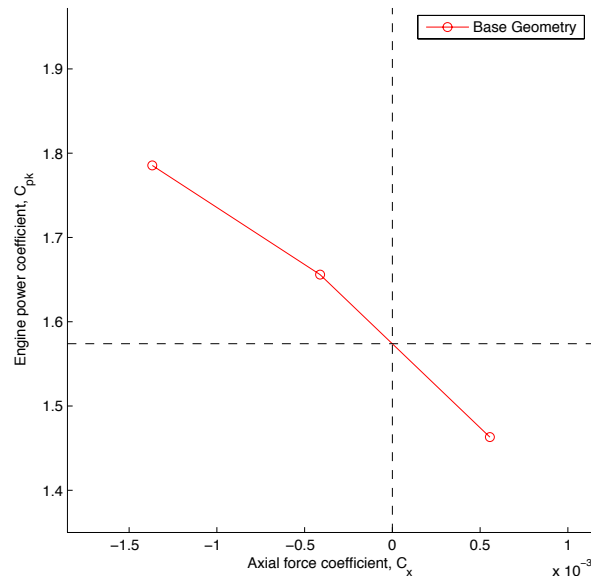
Figure 17: Axial force coefficient vs engine power coefficient, baseline geometry, (Re$_c$=5 million, M=0.85, α = 2°).
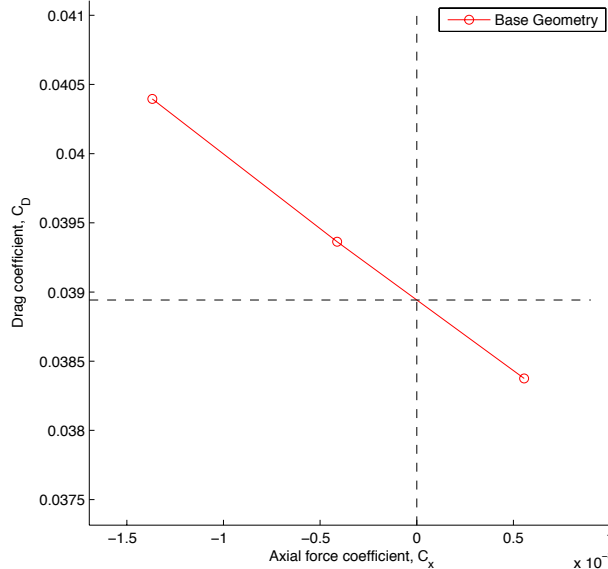
Figure 18: Axial force coefficient vs. drag coefficient, baseline geometry, (Re$_c$=5 million, M=0.85, α = 2°).

American Institute of Aeronautics and Astronautics
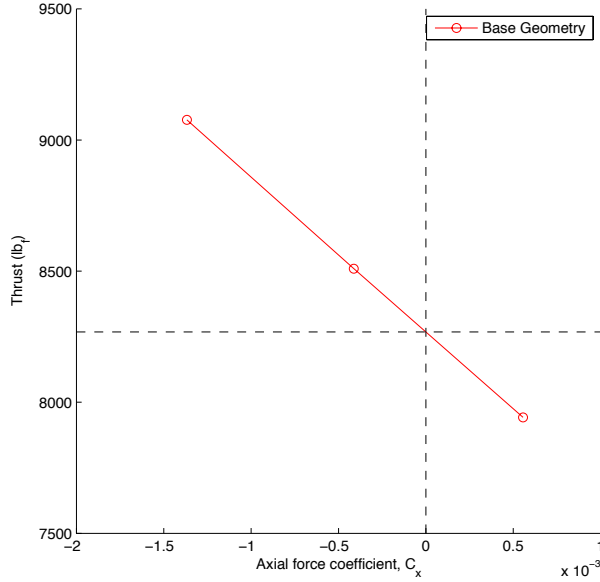
Figure 19: Axial force coefficient vs. thrust (lbf), baseline geometry, (Re$_c$=5 million, M=0.85, $\alpha = 2°$).

From the data, an engine power coefficient of C_{P_k} = 1.574, drag coefficient of C_D = 0.03894, and total thrust of 8268.17 lbf for the semispan baseline geometry at cruise conditions are computed. In addition, a nominal value of C_L = 0.378 was calculated across all engine conditions.

XII.   BLI Geometry – Boundary Layer & Actuator Disk Implementation

In addition to the coefficients computed above, it is also necessary to investigate the developing boundary layer and wake produced by the aircraft in order to implement a BLI system. The boundary-layer thickness, δ, is defined as the normal distance from the geometry to a point where the local flow velocity is ninety-nine percent of free-stream velocity

$$u(y) = 0.99u_\infty \tag{24}$$

At the defined cruise condition, the free-stream velocity is 822.8 ft/s. Therefore, from Eq. (24), the edge of the boundary layer occurs at a point normal to the geometry where $u < 814.6$ ft/s.
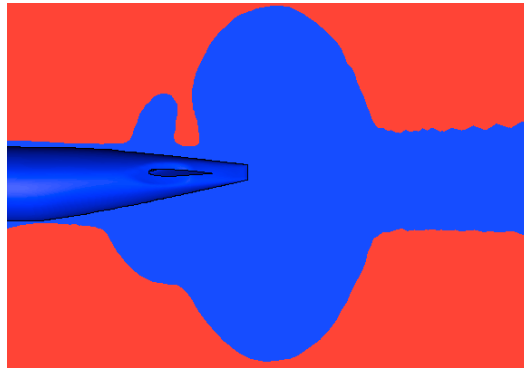
Figure 20: Velocity contour plot with boundary-layer shown in blue, where $u < 814.6$ ft/s .

Fig. 20 presents a contour plot of the empennage and aft end of the fuselage with $u < 814.6$ ft/s in blue and free-stream velocity in red. From this, it can be seen that the boundary layer is developing along the length of the fuselage along with the wake behind the aircraft. Unfortunately, there is an expansion area located at the aft end of the fuselage where the actuator disc for the BLI system is to be placed. This expansion area makes it difficult to pick out the exact location of the boundary layer, so an approximation for the boundary layer thickness must be used. The

boundary layer/wake thickness was approximated following the contour of the developing boundary layer along the fuselage and extending this contour out into the wake region as shown by the black lines in Fig. 21.
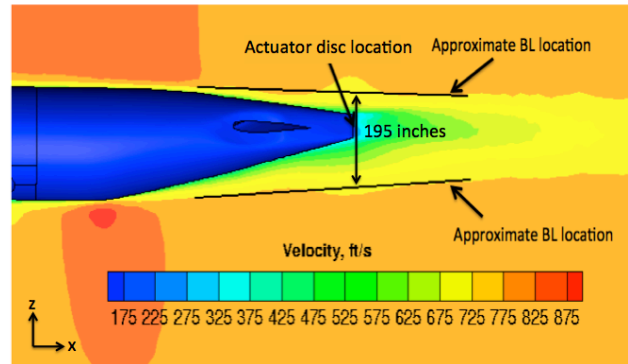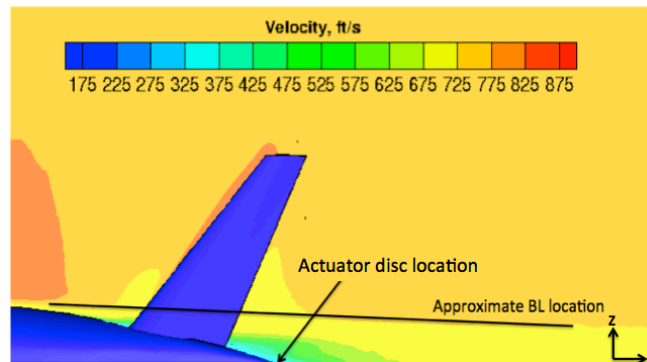

Figure 21: Velocity contour plot with approximate boundary layer and actuator disc location, x-z view, (Re$_c$=5 million, M=0.85, α=2°).

The actuator disc is placed at the center of the aft end of the fuselage as shown in Fig. 21. At this location, the boundary layer/wake is approximately 195 inches thick in the z direction.

Figure 22: Velocity contour plot with approximate boundary layer and actuator disc location, x-y view, (Re$_c$=5 million, M=0.85, α=2°).

Fig. 22 shows a top-down view of the developing boundary-layer and wake. There is some interference from the tail; however, the boundary-layer thickness at the actuator disc location can again be approximated by following the contour of the boundary layer further up the fuselage. At the actuator disc location, the boundary-layer/wake is approximately 91 inches thick in the y direction.

As stated previously, for the purposes of this work, the slower-moving boundary-layer flow is ingested and accelerated to match the free-stream velocity. Since the exit velocity of the disc is designed to be free-stream velocity, there is no need to ingest free-stream air in this application. The radius of the disc can therefore be constrained so that it is not ingesting free-stream air, as areas of the disc in the free-stream would generate thrust by accelerating the flow to above free-stream velocity. As shown in Figs. 21and 22, the boundary layer and wake are not uniform in radius at the actuator disc location. Therefore, the radius of the disc is further confined to be the smallest distance from the center of the disc to the edge of the approximate boundary-layer edge location in any direction.
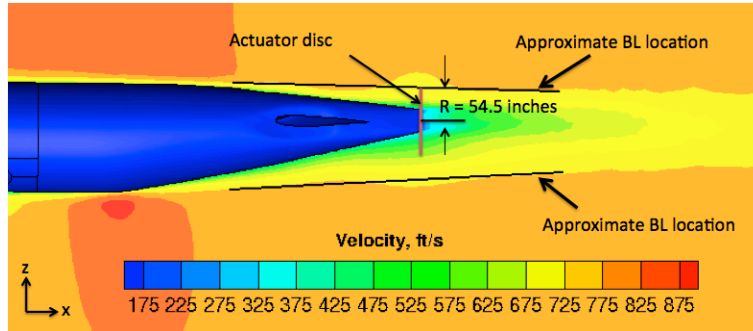
Figure 23: Velocity contour plot showing actuator disc constraint, x-z view, (Re$_c$=5 million, M=0.85, α=2°).

The constraining distance is calculated to be approximately 54.5 inches, which is the distance from the center of the disc to the upper edge of the approximated boundary layer in the z direction, as shown in Fig. 23. For the full model, this gives the actuator disc an area of 64.8 ft^2, with the ingested boundary-layer having a mass-weighted velocity of 528.3 ft/s and mass-flow rate of 21.96 slugs/s, which will allow for the ingestion of approximately 38% of the boundary-layer and wake by area and 32% of the boundary layer by mass-flow rate. For comparison, the same actuator disc placed in the free-stream has a mass-flow rate of 33.4 slugs/s.
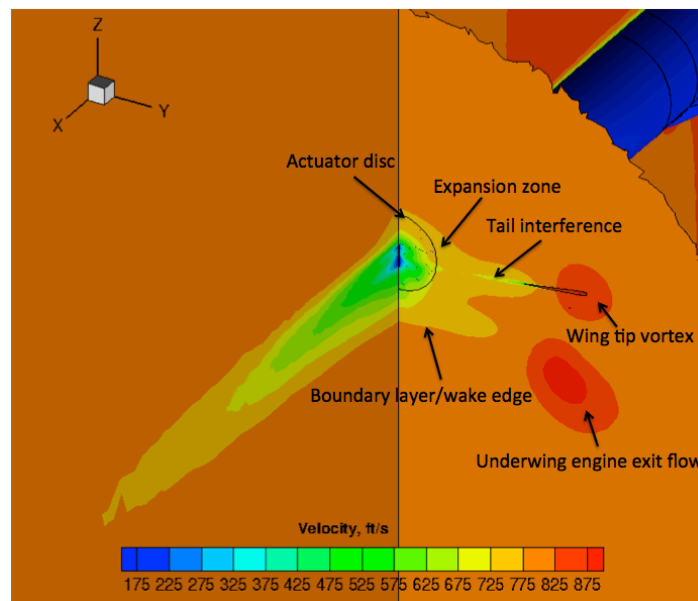
Figure 24: Velocity contour plot with iso-slice at actuator disc location, (Re$_c$=5 million, M=0.85, α=2°).

Although in an ideal situation 100% of the boundary layer would be ingested, since the maximum exit velocity of the BLI system is constrained to be equal to free-stream velocity, there is a diminishing return on how large the system is versus how much benefit can be derived from it. Using the definition of a boundary layer given in Eq. (37) and the general thrust equation from Eq. (2), it is certainly possible to take flow at 99% u_∞, and generate thrust by imparting a slight acceleration. However, far more thrust and therefore net benefit can be generated by taking the slower moving flow found deeper in the boundary-layer and accelerating that to match u_∞, since this would create a larger Δu. The 'sweet spot' for how much of the boundary layer to ingest is largely dependent on the type of propulsion system, how efficient the system is, and what velocity constraints, if any, are placed on the exit flow; however, this is not the focus of this study. In addition, the larger the BLI system is, the larger the potential weight and drag penalties of implementing the system will be.

As can be seen in Fig. 24 above, the actuator disc in this case is not ingesting the full boundary layer, shown in yellow, as the location and size of the actuator disc are constrained by the approximated boundary-layer edge. However, the disc is ingesting a large portion of the slowest boundary-layer flow, shown in green and blue. This

18
American Institute of Aeronautics and Astronautics

should allow for a good approximation of the net benefit of BLI and reduction in power savings without being too idealistic as to be unreasonable in the real world.
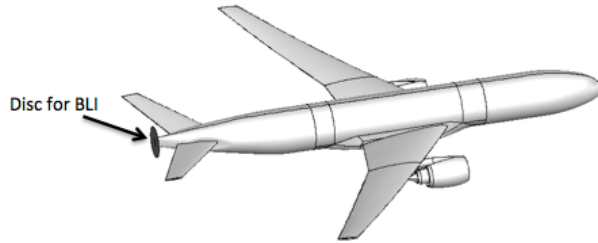

Figure 25: Common Research Model (CRM) with BLI disc

Using Eq. (2), the ingested boundary-layer mass weighted velocity of 528.3 ft/s as the inlet velocity, the mass flow rate of 21.96 slugs/s and constraining the exit velocity to match free-stream velocity, or 822.8 ft/s, the actuator disc is expected to produce 1,454 lbf of thrust, approximately 8.8% of the total thrust required for cruise.

XIII.   BLI Geometry Results – First Iteration

For the initial BLI system, an open, full actuator disc as discussed previously was implemented on the full span CRM directly downstream of the fuselage, with no alterations to the fuselage itself. As shown in Fig. 25, the disc, which is a zero-thickness inviscid surface, was displaced approximately one inch from the back end in order to allow for viscous grid generation.
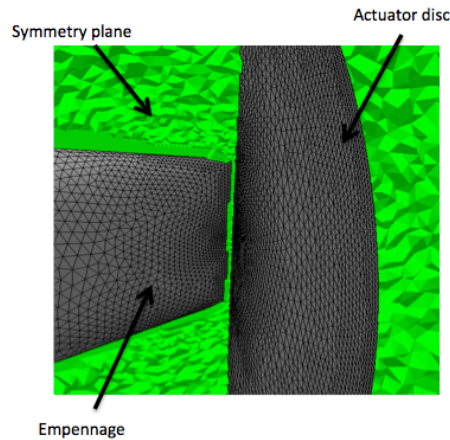
Figure 26: Viscous grid generation near aft end of fuselage with actuator disc.

The grid size for the full-span model was increased to approximately 101.6 million tetrahedral cells with an average y+ value of < 1. The solution was run for a total of fourteen thousand iterations using first-order spatial accuracy for the first two thousand iterations in order to overcome any initial transients in the model and second-order accuracy for the last twelve thousand iterations. Solution convergence was assessed by tracking the convergence parameter using the L2-norm solution residual of all flow variables, $\log(r/r_0)$, versus iteration, as shown in Fig. 27.

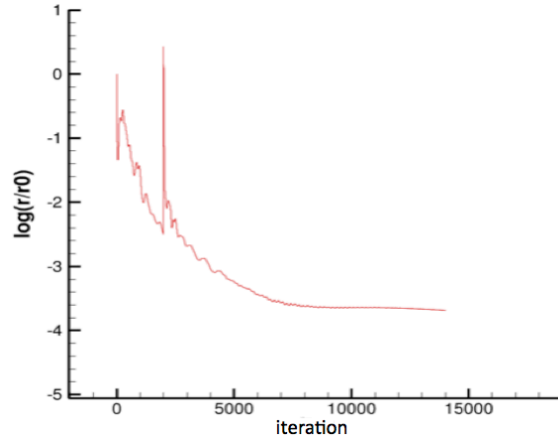American Institute of Aeronautics and Astronautics

Figure 27: L2-norm solution convergence for BLI model.

A uniform step pressure increase was imposed across the surface of the actuator disc. This pressure increase was calculated internally in USM3D using the thrust coefficient outlined in Eq. (38), the free-stream Mach number, M_∞, and user input for advance ratio, J.

$$\Delta C_{p,disc} = \frac{C_T * M_\infty^2}{J^2} \tag{38}$$

An advance ratio of 0.7 was chosen based on the radius of the actuator disc in order to keep the 'tips' of the disc subsonic. Figs. 28 and 29 show contour plots of the pressure coefficient, C_p, for the baseline and BLI geometries, respectively.
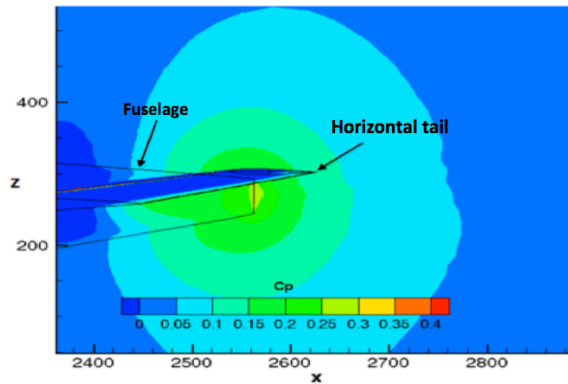
Figure 28: C_p contour plot, baseline geometry, z-x plane, (Re$_c$=5 million, M=0.85, α=2°).
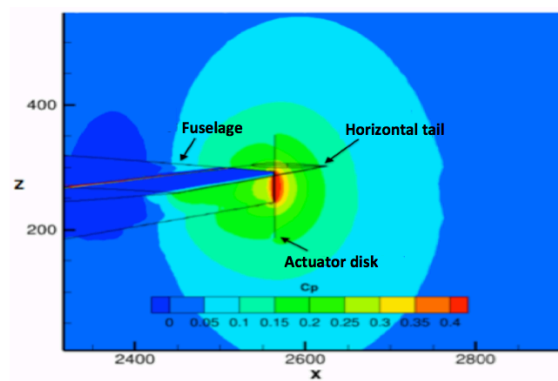
Figure 29: C_p contour plot, BLI geometry, z-x plane, (Re$_c$=5 million, M=0.85, α=2°).

American Institute of Aeronautics and Astronautics

Fig. 29 shows the actuator disc is imparting a slight pressure jump to the incoming flow with the highest C_p occurring on the empennage where the geometry terminates abruptly. As can be seen in Figs. 21 and 22, this abrupt end to the geometry causes a low velocity zone and large wake to develop behind the aircraft, contributing to an increase in drag and engine power requirements. Figs. 30 and 31 show C_p contour plots of the 'in' and 'out' faces of the actuator disc, respectively. Again, the actuator disc is shown to be imposing a pressure jump on the incoming flow, with the highest C_p occurring at the center of the disc where the geometry terminates.
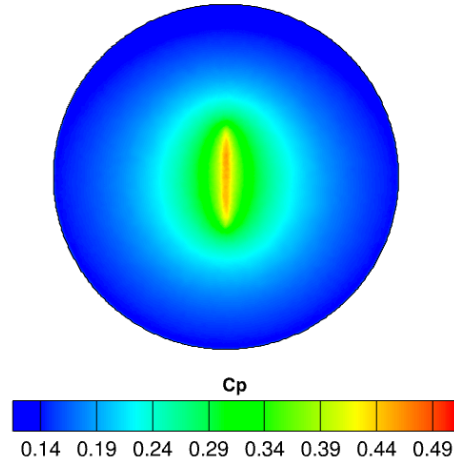
Figure 30: C_p contour plot, actuator disc 'in' face, (Re$_c$=5 million, M=0.85, α=2°).

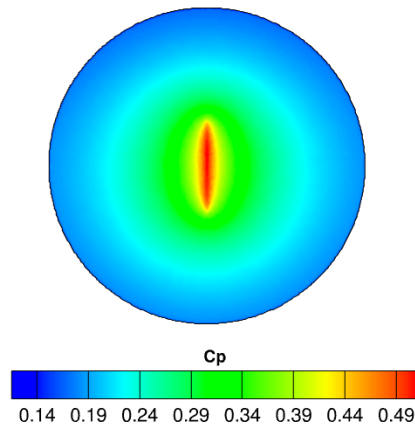
Figure 31: C_p contour plot, actuator disc 'out' face, (Re$_c$=5 million, M=0.85, α=2°).

Fig. 32 shows a velocity contour plot of the flow coming into the actuator disc. From Eq. (24), any flow where u < 814.6 ft/s is by definition, boundary-layer flow. From the contour plot, it is evident that the actuator disc is entirely immersed in the boundary-layer/wake of the aircraft; however, the velocity profile is not uniform. The top portion of the actuator disc has the fastest moving flow, with a maximum velocity of 775.8 ft/s. Relative to the top portion of the actuator disc, the sides and bottom have slower-moving flow due to interference from the horizontal-tail wake and the taper from the bottom of the fuselage. The center of the actuator disc where the fuselage comes to an end has a minimum velocity of 159.8 ft/s, approximately 19.4% that of free-stream velocity. The mass weighted velocity at the actuator disc exit is 630.9 ft/s, an increase of 102.5 ft/s over the baseline geometry.
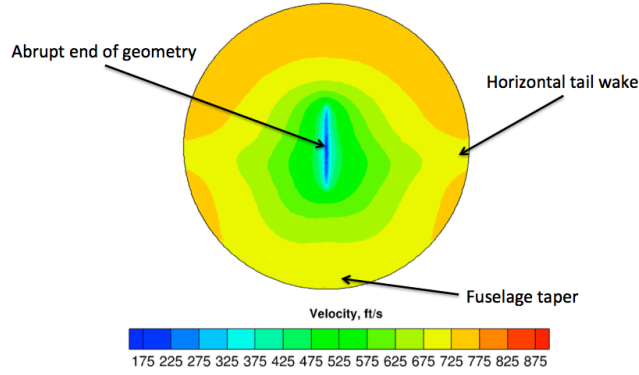
American Institute of Aeronautics and Astronautics

Figure 32: Velocity contour plot, BLI geometry actuator disc 'in' face, (Re_c=5 million, M=0.85, α=2°).

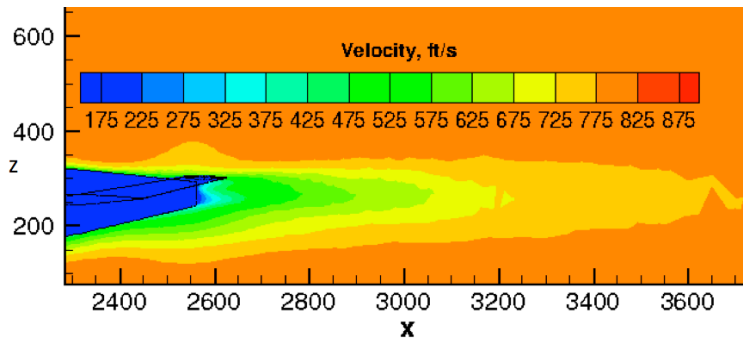Figs. 33 and 34 show velocity contour plots of the wake for the baseline and BLI geometries.

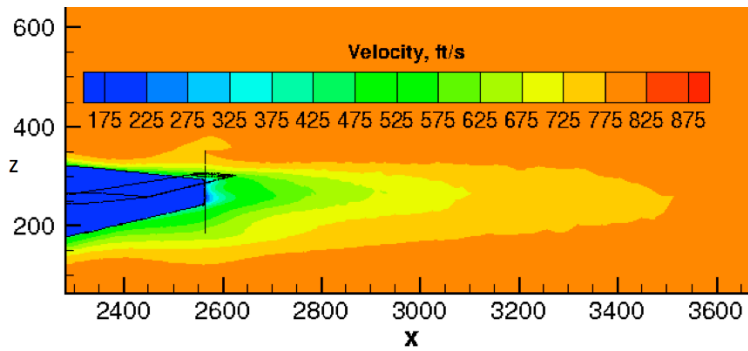Figure 33: Velocity contour plot of wake, baseline geometry, (Re_c=5 million, M=0.85, α=2°).

Figure 34: Velocity contour plot of wake, BLI geometry, (Re_c=5 million, M=0.85, α=2°).

From these figures, it is evident that implementing the actuator disc does have a moderate effect on the aircraft wake, although it is not completely eliminated as intended. Fig. 34 shows an isometric view of the wake and actuator disc.
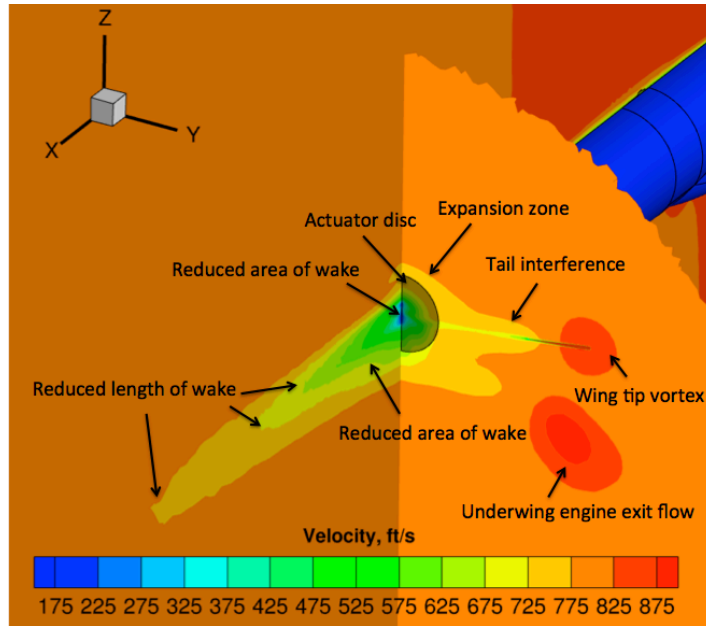
Figure 35: Velocity contour plot with slice at actuator disc location, BLI geometry, (Re$_c$=5 million, M=0.85, α=2°).

The actuator disc appears to be fully immersed in the wake/boundary-layer, although there is a large portion of the wake/boundary-layer flow that is not ingested by the actuator disc. Compared to the baseline geometry, shown in Fig. 24, the lower velocity regions, particularly the green and blue, which represent the lowest velocity areas, are all reduced in size and length. In addition, the overall length of the wake is reduced.

The engine power coefficient, C_{p_k}, and axial force coefficient, C_x, were calculated for the BLI geometry and plotted against previous results for the baseline geometry. Since it was not possible to refine the engine model any further between the data points, C_{p_k} at the exact cruise point of $C_x = 0$ was interpolated from available data.
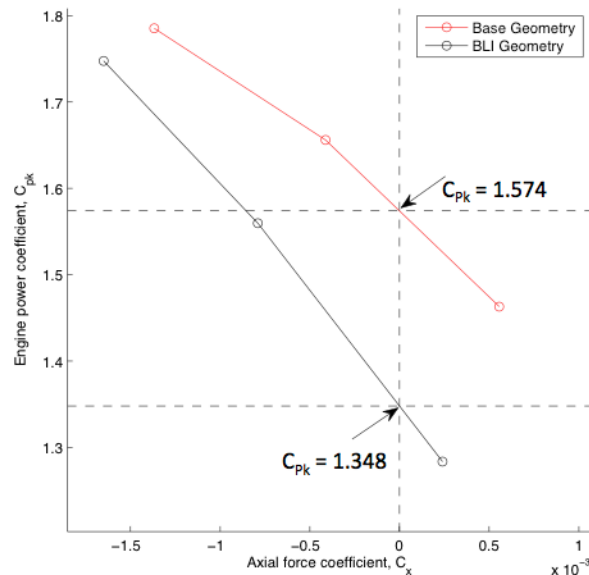

Figure 36: Axial force coefficient versus engine power coefficient, baseline and BLI geometries,
(Re$_c$=5 million, M=0.85, $\alpha = 2°$).

As shown in Fig. 36, introducing the actuator disc as the BLI system reduces the engine power coefficient, indicating a net reduction in the overall propulsion power required by the aircraft to achieve cruise compared to the baseline geometry. The BLI configuration is shown to require 14.4% less propulsive power relative to the baseline

geometry. Fig. 37 shows a plot of the drag coefficient for both the baseline and BLI geometries. As mentioned previously, drag was computed only over the solid surfaces.
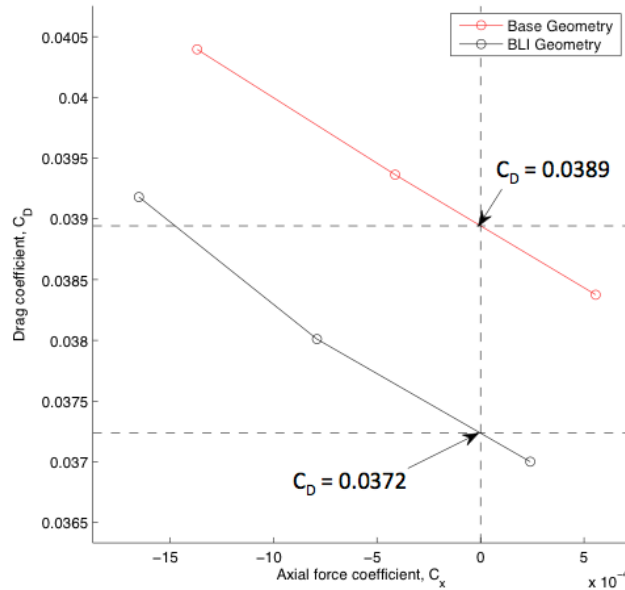

Figure 37: Axial force coefficient versus drag coefficient, baseline and BLI geometries,
(Re_c=5 million, M=0.85, α = 2°).

Fig. 37 shows that there is a reduction in drag for the BLI geometry, likely due to the actuator disc accelerating the flow slightly as it nears the end of the fuselage, thus re-energizing the boundary-layer. A nominal C_L value of 0.374 was calculated for the BLI geometry over all engine conditions, a reduction of 0.04 compared to the baseline geometry.

XIV.   BLI Geometry Results – Second Iteration

A preliminary attempt to improve the benefits of the actuator disc BLI system was made using the Constrained Direct Iterative Surface Curvature[26] (CDISC) design method by slightly altering the back portion of the fuselage near the actuator disc. CDISC works by extracting the surface coordinates and pressure coefficients from an initial analysis. Specific design target stations (e.g., a portion of the wing, an area of the fuselage) as well as target pressures, flow, and geometry constraints for these areas are designated by the user. CDISC then alters the geometry by stretching, shrinking and moving the surface mesh cells in an attempt to match the desired target pressures along the designated design target stations. Once the surface geometry is altered, the volume grid is then modified based on the surface geometry changes and input back into the flow solver for further analysis. This iterative process repeats until the extracted surface pressures match input target pressures[26]. For this design attempt, four target stations were used, located every 90 degrees circumferentially, starting from the top of the fuselage.
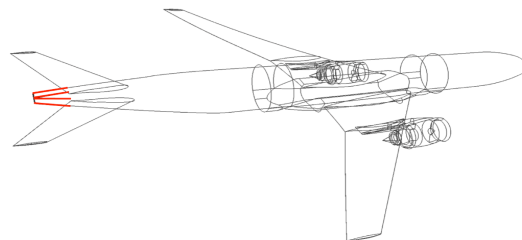

Figure 38: CDISC design stations.

Fig. 38 shows the design stations in red, beginning just behind the trailing edge of the horizontal tail and extended to the end of the fuselage. The final vertical thickness of the fuselage is held constant so that the geometry changes are not too drastic, as this is only a first-round design attempt.

The surface pressures for the original BLI geometry were extracted, and a design constraint was imposed on C_p over the top and bottom of the fuselage to increase the average surface pressure of the design area. By increasing C_p in this area, the idea is that the flow will 'squeeze' the fuselage, causing a net forward force, similar to pinching an ice cube and having it shoot forward. Normally, this geometry change would be expected to decelerate the flow, increasing the boundary-layer and wake. However, as the BLI system is located close by, any decrease in velocity should actually be beneficial to the BLI system and contribute to the overall power reduction. No design constraints were imposed on the sides of the fuselage. However, as CDISC blends the geometry changes between the stations, the surface mesh was altered slightly at these locations. Fig. 39 below shows the side view (left) of the original surface mesh (blue) and redesigned CDISC mesh (red) as well as a top view (right).
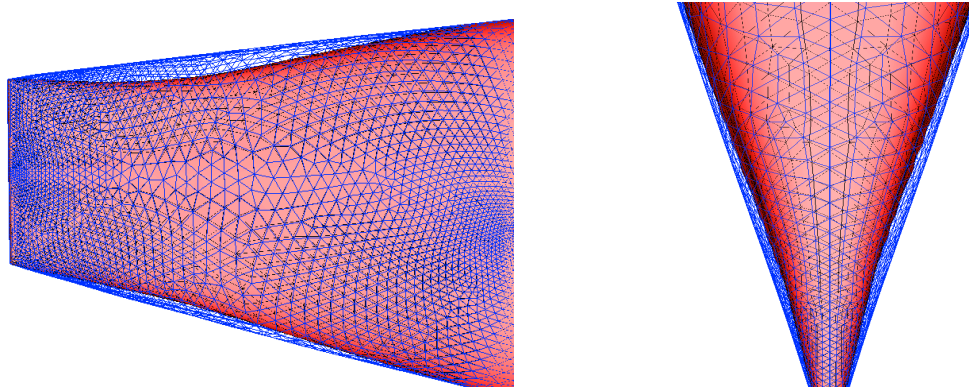

Figure 39: Original (blue) and updated (red) mesh, side view (left), top view (right).

Figs. 40 and 41 show close-up velocity contour plots near the redesigned areas in both the original and updated BLI geometries.
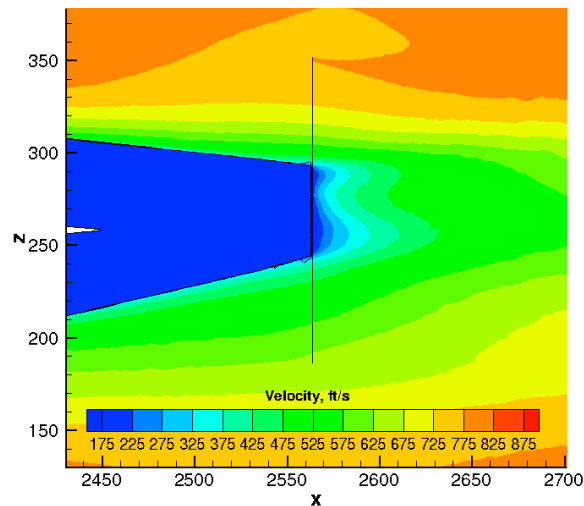

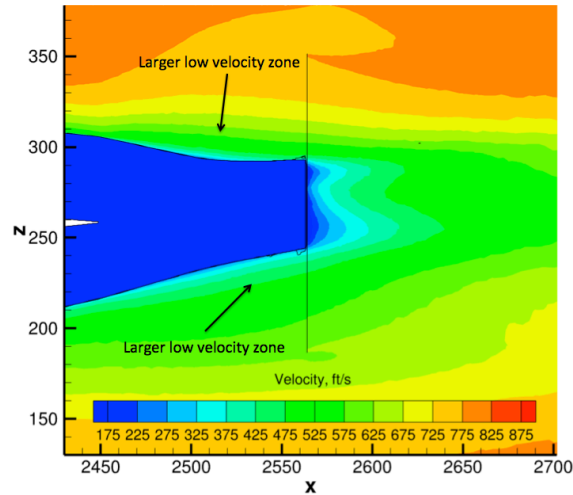Figure 40: Velocity contour plot, close up - original BLI geometry, (Re$_c$=5 million, M=0.85, $\alpha = 2°$).

Figure 41: Velocity contour plot, close up – CDISC redesigned BLI geometry, (Re$_c$=5 million, M=0.85, α = 2°).

For the CDISC redesigned BLI geometry, there is a small increase in the area of the low velocity zone, shown in green, both on the upper and lower portions of the aft fuselage. Although, since the upper area went through a more drastic change (relatively), the change is more noticeable compared to the lower surface. There was no noticeable change in the wake flow for the redesigned geometry.

Again, the engine power coefficient, C_{p_k}, and axial force coefficient, C_x, were calculated for the redesigned BLI geometry and plotted against previous results for both the baseline and original BLI geometries.
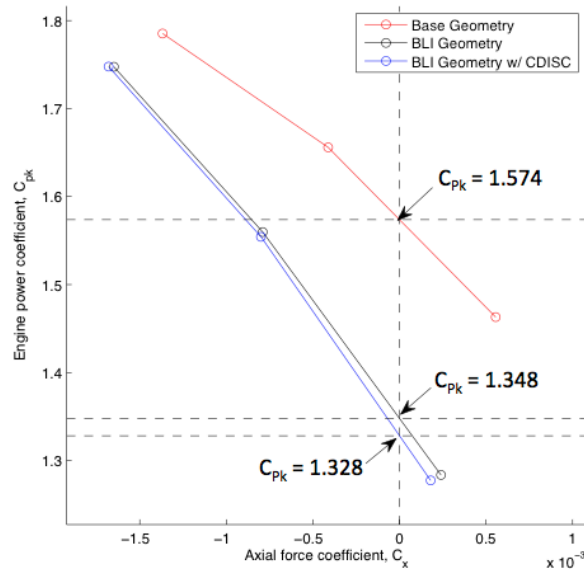

Figure 42: C_x versus C_{P_k}, baseline and BLI geometries, (Re$_c$=5 million, M=0.85, α = 2°).

As Fig. 42 shows, the geometry modifications introduced by CDISC led to a slight decrease in the engine power coefficient at cruise. The redesigned BLI configuration is shown to require 15.6% less propulsive power relative to the baseline geometry, a 1.4% improvement over the original BLI geometry.
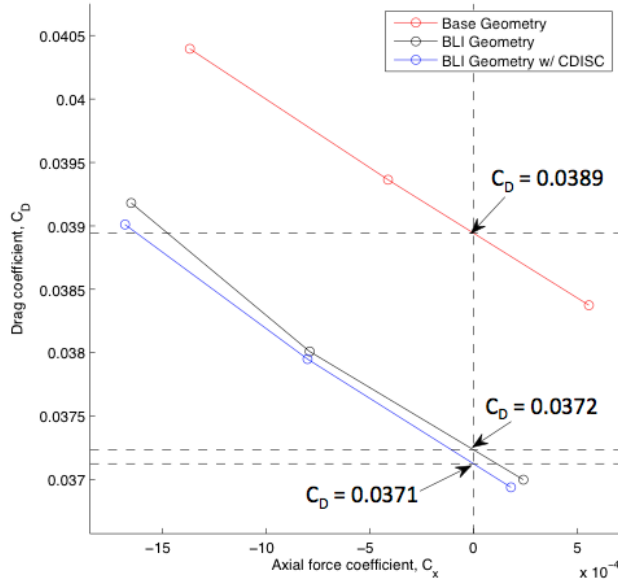
Figure 43: C_x versus C_D, baseline and BLI geometries, (Re$_c$=5 million, M=0.85, α = 2°).

Fig. 43 is a plot of the drag coefficient for all geometries at this point. There is a slight reduction in drag of approximately eighteen counts for the redesigned BLI geometry compared to the original BLI geometry. A nominal C_L value of 0.373 was calculated for the CDISC BLI geometry over all engine conditions, a reduction of 0.05 compared to the baseline geometry.

Further alterations to the fuselage were not possible at this time due to a combination of geometric and grid constraints. CDISC works by stretching and shrinking cells on the surface mesh. This stretching and shrinking is then propagated out into the volume grid. However, since the actuator disc was located so close to the back end of the fuselage in this case, stretching and shrinking the cells in this area resulted in negative volume cells and cells with crossed faces, which were not able to be removed. In order to correct this, it would be necessary to either regenerate the grids with a much finer mesh in the actuator disc area, which would allow surface mesh changes to propagate out into the volume grid without the creation of negative cells, or else the relocation of the actuator disc further away from the end of the fuselage.

XV.   CDISC Geometry Without BLI Results

As it is unclear at this point whether the additional reduction in engine power requirements at cruise for the CDISC BLI geometry compared to the first iteration BLI configuration arises from improved performance of the fuselage itself, an increased benefit derived from the BLI system, or else a combination of both, an additional study was done to determine where this benefit comes from. To this end, the actuator disc representing the BLI system was removed from the CDISC geometry, simulations were re-run at the same cruise and engine conditions and results were plotted against previously obtained data.
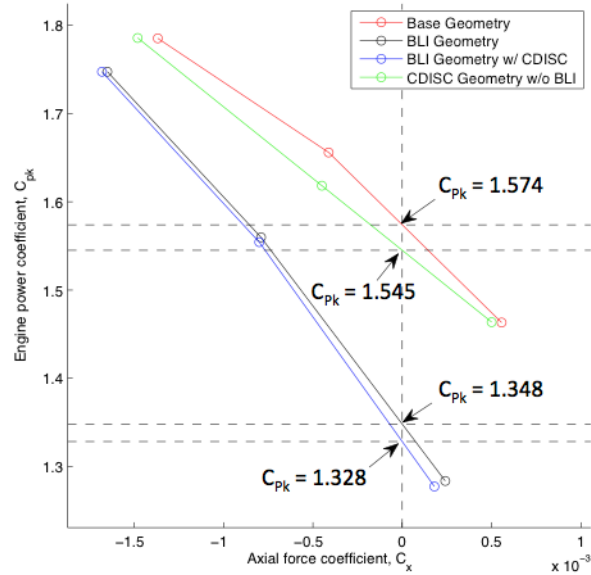
Figure 44: C_x versus C_{P_k}, all geometries, (Re_c=5 million, M=0.85, $\alpha = 2°$).

From Fig. 44 above, the alterations made to the fuselage without the BLI system resulted in a cruise power reduction of 1.8% over the baseline. However, as stated previously, these same changes resulted in a power reduction of only 1.4% between BLI geometries. Since there is less of a power reduction between BLI geometries compared to the non-BLI geometries, it is safe to say that the additional reduction in engine power is a result of the changes to the fuselage itself and not necessarily from improved performance of the BLI system.

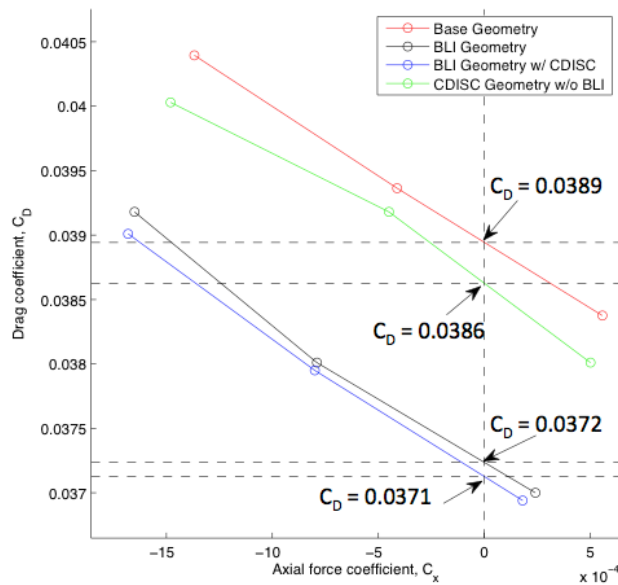
Figure 45: C_x versus C_D all geometries, (Re_c=5 million, M=0.85, $\alpha = 2°$).

Fig. 45 is a plot of the drag coefficient for all geometries. There is a small reduction in drag of approximately 3 counts between the non-BLI geometries. A nominal C_L of 0.377 was calculated as well over all engine conditions, a reduction of 0.01 compared to the baseline.

XVI.   Conclusions and Future Work

Unstructured grid-based computational solutions encompassing multiple geometries and several different computational tools have been demonstrated, along with a methodology for evaluating the benefit of Boundary-Layer Ingestion for conventional aircraft. GridTool and VGRID advancing front grid generation software were used to generate unstructured tetrahedral grids for analysis.

The USM3D flow solver has been verified against both previous computational results, and data gathered during earlier experiments using the Common Research Model geometry. The NPSS software has been shown to provide useful inputs for CFD analysis, allowing for the realistic modeling of turbojet engines in this application. In addition, CDISC has been shown to be a useful tool for geometry modification and design.

From the analysis above, it is evident that the combination of BLI both with and without fuselage shaping provides a significant reduction in terms of propulsive power required for cruise. This benefit has been shown to be the result of a combination of wake filling and using the slower moving boundary-layer flow for propulsion instead of free-stream air, as outlined in Section I. It is important to note that as the wake was only moderately reduced by the introduction of the BLI system, the majority of the benefit of BLI, in terms of cruise propulsive power reduction, seems to stem from the reduction in velocity of the incoming flow into the propulsor.

Table 4: Summary of data

Geometry	C_{Pk}	Power Reduction	C_D	C_L
Baseline	1.574	-	0.0389	0.378
BLI	1.348	14.4%	0.0372	0.374
BLI w/ CDISC	1.328	15.6%	0.0371	0.373
CDISC w/o BLI	1.545	1.8%	0.0386	0.377

The current BLI propulsor model imparts a uniform pressure jump across the actuator disc, which may not be entirely accurate when the fan encounters an inlet distortion. An actual fan would impart a smaller pressure rise to the portion of the flow with higher stagnation pressure and larger pressure rise to the portion of the fluid with lower stagnation pressure. These differences in pressure rise across the fluid, and could affect flow behavior upstream of the actuator disc as well as the exhaust flow. The implementation of a more advanced actuator disc boundary condition with a radially varying pressure distribution is recommended to improve accuracy of results for BLI implementation.

As this study used a nondescript, open actuator disc propulsion system to model the BLI system, the implementation of a more real-world propulsion system would improve the trustworthiness of calculated potential benefits as well as allow for evaluation of system-dependent losses. A trade study to determine a list of viable candidates (e.g., open propeller, ducted electric fan, small turbofan engine) using current technology, or the development of a specifically designed propulsion system and implementation of said system, would yield more accurate results on the exact amount of power savings from the use of BLI as it is implemented here. The use of a full propulsion system model over the representative actuator disc would also allow for assessments of any weight penalties or reduction in benefits from flow distortion through the inlet, fan face, and/or nacelle depending on the chosen system as these are not modeled in this study.

In order to better understand the prospective power savings and how a BLI system might affect other subsystems and flight variables, additional computations should be conducted at alternate operating conditions and flight regimes.

Overall, airframe propulsion integration and the implementation of a BLI system present a complex and challenging design optimization problem. Aircraft engines are sized for take off, with the operating cruise point being a percentage of full throttle. By introducing BLI, it may be possible to scale down the size of the engines, thus reducing wetted area and overall drag, which would increase the benefit of BLI at a system level even further. However, the addition of a BLI system will likely add weight to the aircraft, which will then require more overall thrust at take off. If the BLI system does not produce at least that much additional thrust, the size of the wing mounted engines as well as the wing area would need to be increased, further increasing weight and cost. Also, keeping the engine sized the same for take off but throttling down to a lower operating cruise point may cause the propulsive efficiency to decrease and specific fuel consumption to increase; however, the total mission fuel would

American Institute of Aeronautics and Astronautics

likely decrease. In addition, at a lower operating cruise point, harmful environmental emissions should decrease due to lower combustor temperature and overall pressure ratio of the engine.

A recent investigation by Welstead and Felder[30] into BLI from an overall design and propulsion architecture standpoint, as apposed to the aerodynamic, CFD perspective used in this work, examined some of the potential issues with BLI outlined above. Their work evaluated a turboelectric commercial transport architecture with two underwing turbofan engines and a rear fuselage, axisymmetric, boundary-layer ingesting fan. Results from this study indicate that the addition of BLI would actually allow for the reduction of underwing engine wetted area, along with overall aircraft weight, as well as a fuel burn reduction of 7 to 12 percent, thus invalidating some of the potential issues of BLI highlighted previously.

The purpose of this work is not to declare whether or not BLI should be implemented in the real world, but instead serve as a starting point for designing and evaluating the potential benefit of a BLI system in this application. This analysis shows that implementing an ideal BLI system in the above fashion can provide a significant benefit in terms of propulsive power reduction, and therefore warrants further, more detailed study. However, this analysis does not take into account systemic losses that would be dependent on actual engine design and implementation. In addition, this work does not look into the structural effects that implementing a BLI system might have. Ideally, the entire system, including required thrust, wing area, aircraft weight, and engine design variables would be 'clean sheet' designed to meet the desired design goals.

XVII. Acknowledgements

References

[1] Smith, A. M. O. and Roberts, H., "The Jet Airplane Utilizing Boundary-layer Air for Propulsion," *Journal of the Aeronautical Sciences (Institute of the Aeronautical Sciences)*, vol. 14, 1947, pp. 97–109.

[2] F. R. Goldschmied, "On the Aerodynamic Optimization of Mini-RPV and Small GA Aircraft," *2nd Applied Aerodynamics Conference*, 1984.

[3] Roepke, Joshua. "An Experimental Investigation of a Goldschmied Propulsor." MSc Thesis, California Polytechnic State University, 2012.

[4] Douglass, W., "Propulsive Efficiency with Boundary-Layer Ingestion," McDonnell Douglas Report MDC J0860, 1970.

[5] Daggett, David L., Ron Kawai, and Doug Friedman. "Blended Wing Body Systems Studies: Boundary-Layer Ingestion Inlets with Active Flow Control." *NASA CR*-212670, 2003.

[6] Uranga, A., Drela, M., Greitzer, E., Titchener, N., Lieu, M., Siu, N., Huang, A., Gatlin, G. M., and Hannon, J., "Preliminary Experimental Assessment of the Boundary-Layer Ingestion Benefit for the D8 Aircraft," *52nd Aerospace Sciences Meeting*, Oct. 2014, AIAA-2014-0906.

[7] Pandya, S. A., Uranga, A., Espitia, A., and Huang, A., "Computational Assessment of the Boundary-layer Ingesting Nacelle Design of the D8 Aircraft," *52nd Aerospace Sciences Meeting*, Oct. 2014, AIAA-2014-0907.

[8] Sabo, K. M., and Drela, M., "Benefits of Boundary-Layer Ingestion Propulsion, "*53rd AIAA Aerospace Sciences Meeting*, Mar. 2015, AIAA-2015-1667.

[9] Berrier, B., and Allan, B., "Experimental and Computational Evaluation of Flush-Mounted, S-Duct Inlets," *42nd AIAA Aerospace Sciences Meeting and Exhibit*, May 2004, AIAA-2004-764.

[10] Rodriguez, D., "A Multidisciplinary Optimization Method for Designing Boundary-layer Ingesting Inlets," *Journal of Aircraft,* vol. 46, No. 3, 2009, pp. 883-894.

[11] Smith, L. H., "Wake Ingestion Propulsion Benefit," *Journal of Propulsion and Power*, vol. 9, 1993, pp. 74–82.

[12] Arntz, A., Atinault, O., Destarac, D., and Merlen, A., "Exergy-based Aircraft Aeropropulsive Performance Assessment: CFD Application to Boundary-Layer Ingestion," *32nd AIAA Applied Aerodynamics Conference*, 2014, AIAA-2014-2573.

[13] Plas, A., Crichton, D., Sargeant, M., Hynes, T., Greitzer, E., Hall, C., and Madani, V., "Performance of a Boundary-layer Ingesting (BLI) Propulsion System," *45th AIAA Aerospace Sciences Meeting and Exhibit*, Aug. 2007, AIAA-2007-450

[14] Küchemann, D., and Johanna W., *Aerodynamics of propulsion*. Vol. 2. McGraw-Hill, 1953, pp. 205-209.

[15] Blumenthal, B., "Computational Investigation of a Boundary-Layer Ingestion Propulsion System for the Common Research Model.", MS Thesis, Pennsylvania State University, May 2016.

[16] Vassberg, J., Dehaan, M., Rivers, M., and Wahls, R., "Development of a Common Research Model for Applied CFD Validation Studies," *26th AIAA Applied Aerodynamics Conference*, 2008, AIAA-2008-6919.

[17] Yamamoto, K., Tanaka, K., and Murayama, M., "Comparison Study of Drag Prediction for the 4th CFD Drag Prediction Workshop using Structured and Unstructured Mesh Methods," *28th AIAA Applied Aerodynamics Conference*, 2010, AIAA-2010-4222.

[18] Turner, M. G., Reed, J. A., Ryder, R., and Veres, J. P., "Multi-Fidelity Simulation of a Turbofan Engine With Results Zoomed Into Mini-Maps for a Zero-D Cycle Simulation," *Volume 2: Turbo Expo 2004*, 2004.

[19] "TetrUSS: USM3D Overview." *TetrUSS: USM3Dns Online Manual*. NASA Langley Research Center, 8 Aug. 2003. Web. 1 Feb. 2015. <http://tetruss.larc.nasa.gov/usm3d/overview.html>.

[20] Jones, S., NASA GRC Reference model for 90000 lb thrust class direct-drive turbofan, 2011.

[21] Drela, M., "Power Balance in Aerodynamic Flows," *27th AIAA Applied Aerodynamics Conference*, 2009, AIAA Journal 27, no.7 1761-1771

[22] Pirzadeh, S., "Progress Toward a User-Oriented Unstructured Viscous Grid Generator," *34th Aerospace Sciences Meeting and Exhibit*, 1996, AIAA-1996-0031.

[23] Lytle, John K. "The Numerical Propulsion System Simulation: An Overview." *NASA CR*-209915, 2000.

[24] "Basic NPSS Gas Turbine Engine Modeling." Wolverine Ventures, 10 June 2010. Web. 13 Jan. 2015. <http://www.wolverine-ventures.com/images/pdf/basic_npss.pdf>.

[25] Kirby, M., Barros, P., and Mavris, D., "Enhancing the Environmental Policy Making Process with the FAA's EDS Analysis Tool," *47th AIAA Aerospace Sciences Meeting including The New Horizons Forum and Aerospace Exposition*, May 2009, AIAA-2009-1262.

[26] Campbell, R., "Efficient Viscous Design of Realistic Aircraft Configurations," *29th AIAA, Fluid Dynamics Conference*, 1998, AIAA-1998-2539.

[27] Morrison, J., "Statistical Analysis of CFD Solutions from the Fourth AIAA Drag Prediction Workshop," *28th AIAA Applied Aerodynamics Conference*, 2010, AIAA-2010-4673.

[28] Levy, D., Laflin, K., Vassberg, J., Tinoco, E., Mani, M., Rider, B., Brodersen, O., Crippa, S., Rumsey, C., Wahls, R., Morrison, J., Mavriplis, D., and Murayama, M., "Summary of Data from the Fifth AIAA CFD Drag Prediction Workshop," *51st AIAA Aerospace Sciences Meeting including the New Horizons Forum and Aerospace Exposition*, May 2013, AIAA-2013-0046.

[29] Rivers, M., and Hunter, C., "Support System Effects on the NASA Common Research Model," *50th AIAA Aerospace Sciences Meeting including the New Horizons Forum and Aerospace Exposition*, Sep. 2012, AIAA-2012-0707.

[30] Welstead, J., and Felder, J., "Conceptual Design of a Single-Aisle Turboelectric Commercial Transport with Fuselage Boundary Layer Ingestion." *54th AIAA Aerospace Sciences Meeting*, 2016, AIAA-2016-1027.